Towards Scanning Tunneling Microscopy Measurements on Cuprates in the Presence of a Transport Current

Barquero Pierantoni, Sergio

Towards Scanning Tunneling Microscopy Measurements on Cuprates in the Presence of a Transport Current

THESIS

submitted in partial fulfillment of the
requirements for the degree of

MASTER OF SCIENCE
in
PHYSICS

Author :	Sergio Barquero Pierantoni
Student ID :	s2386089
Supervisor :	Milan Allan
2^{nd} corrector :	Michiel de Dood

Leiden, The Netherlands, March 24, 2021

Towards Scanning Tunneling Microscopy Measurements on Cuprates in the Presence of a Transport Current

Sergio Barquero Pierantoni

Huygens-Kamerlingh Onnes Laboratory, Leiden University
P.O. Box 9500, 2300 RA Leiden, The Netherlands

March 24, 2021

Abstract

Copper oxide superconductors (cuprates) are perhaps among the best known strongly correlated materials. Upon chemical (hole) doping of the antiferromagnetic parent compound, a variety of different electronic phases emerges, including a mysterious pseudogap phase and unconventional superconductivity. Alternatively, forcing a transport current can also induce phase transitions [1–4]. In this thesis, we outline the first steps towards the local characterization of these current-induced electronic properties using low-temperature Scanning Tunneling Microscopy (STM). After studying the viability of these experiments, we define different regions in the doping-current phase diagram suitable for the local characterization of the various phases. The large current densities and accurate doping control needed to reach these regions require the usage of thin samples that were proven hard to manufacture. However, we present the first steps towards a simple fabrication method that allows cleaving thin exfoliated flakes after being stamped on a Si/SiO_2 chip with pre-patterned contacts. After studying and optimizing the cleaving processes of $Bi_2Sr_2CaCu_2O_{8+x}$ flakes onto Gold and Si/SiO_2 we conclude that the presented method is not ideal, and suggest more elaborate methods that include conventional lithography approaches.

Contents

Version of March 24, 2021– Created March 24, 2021 - 12:07

Chapter 1

Introduction

The electronic properties of most metals can be studied using Fermi-liquid (FL) theory. In this framework, the electron interactions are assumed to be weak and are only treated as perturbations from the non-interacting picture. However, the particular chemistry of the copper oxide superconductors (cuprates) conspires to maximize electronic interactions. As a result, a wide variety of electronic phases that cannot be explained using FL theory emerges.

A great body of literature has been developed considering the electronic phases that emerge upon changing the hole content (doping) and temperature of the insulating parent compound of the cuprates [5–7] (see Fig. 2.2). These resulting phases have been proven to be of great interest from both a imdustrial and a fundamental point of view. For instance, the high critical temperature of the unconventional superconducting phase allows for superconducting applications at liquid nitrogen temperature, reducing costs and easing large-scale applications. On the other hand, the linear resistivity observed at the strange metal phase seems to be explained by holographic duality, a theory that asserts mathematical equivalence between strongly interacting quantum field theories and some classical theories of gravity in higher-dimensional curved spacetimes [8].

Forcing a transport current through the cuprates has been recently shown to induce novel electronic phases [1–4] (see Fig. 2.4). Although the properties of these states have been studied using transport and surface-sensitive techniques, there is a lack of local information in these current-induced states. We believe that this local information could shed some light on the microscopic processes induced by a transport current on cuprates, like the motion of vortices or the breaking of Cooper pairs.

Scanning Tunneling Microscopy (STM) has been proven to be a formidable

tool for probing electronic and topographic phases at the local scale. In this thesis, we outline the first steps towards the local characterization of current-induced phases on cuprates using STM. After discussing the viability of STM to probe the electronic (local density of states) and transport (local potential) properties of these current-induced states, we take the first steps towards the fabrication of samples for these kinds of experiments.

Chapter 2

Theory

2.1 Physics Beyond Band Theory : The Cuprates

Band theory correctly predicts the electronic phase (conductor, semiconductor, insulator) of a wide range of materials. Remarkably, this theory is based on an independent electron approximation where the electron-electron interaction is not explicitly taken into account[†]. This is the foundation of the Landau Fermi liquid theory, which addresses the weak electron-electron interaction as a perturbation from the non-interacting picture.

However, there are certain systems where the electron interactions are strong, and can no longer be treated perturbatively; these are the so-called strongly correlated systems. The strong interaction between electrons, together with their low kinetic energy (narrow bandwidth), gives rise to a wide variety of emergent phenomena that cannot be explained within the framework of traditional band theory. Copper Oxides (cuprates) are a great example of strongly correlated systems where emergent phenomena can be studied.

The cuprates are a family of layered materials where the chemistry conspires to maximize the electron-electron interaction. The building block of this family is the CuO_2 plane shown in Fig. 2.1b. These copper oxide planes are separated by electronically inert layers of atoms (Bi, O, Y, Ba, La) forming a perovskite crystal structure. The CuO_2 planes are responsible for the electronic properties whilst the intermediate layers work as electronically inert charge reservoirs.

In the CuO_2 plane (Fig. 2.1a), each copper ion ($Cu^{+2} : [Ar]3d^9 \rightarrow$

[†]In traditional band theory, the e-e interaction is effectively included in the periodic potential

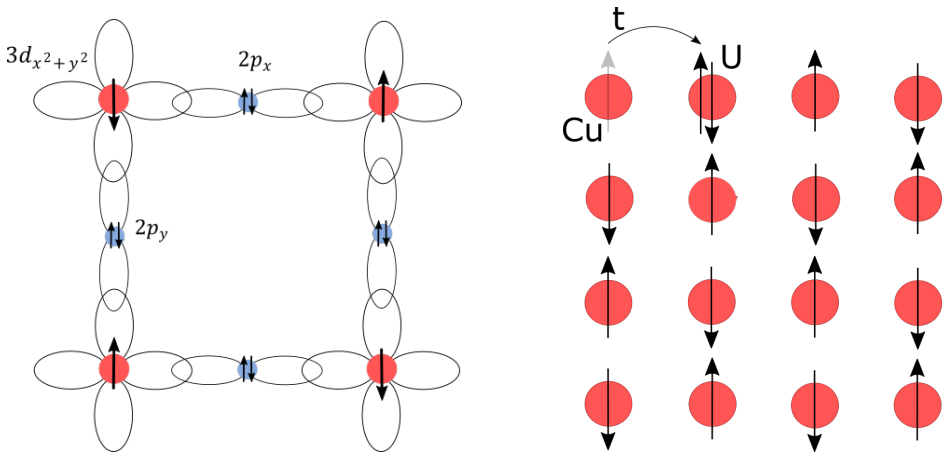

(a) *Cartoon representing the CuO_2 plane* ***(b)*** *Cartoon representing the Mott State*

Figure 2.1: *CuO_2 plane with one $3d_{x^2-y^2}$ electron localized around each Cu atom. If the Coulomb repulsion between electrons (U) is greater than their kinetic energy (t) they will remind localized forming the so-called Mott state.*

half-filled $3d_{x^2-y^2}$ orbital in-plane) binds with four oxygen ions (O^{2-} : $[He]2s^2 2p^6 \rightarrow$ filled $2p_x$, $2p_y$ in-plane). If we try to apply a simple tight-binding model to this CuO_2 plane, we will find it to be conductive with a half-filled band*. However, the system is experimentally found to be insulating. This striking discrepancy between band theory and experiments can be explained taking into account the electron-electron interaction.

The CuO_2 plane was found to belong to a new kind of insulators, the so-called "Mott insulators". Mott insulators are an example of strongly correlated systems where the electron-electron interactions cannot be studied perturbatively and conventional band theory fails. Fortunately Mott proposed a simple physical picture that explains this puzzle. Consider our CuO_2 plane as depicted in Fig. 2.1a where there is one localized electron around each Cu atom. Such electrons can hop into a neighboring copper atom if their kinetic energy (hopping parameter t) is larger than the coulomb repulsion generated by the electron localized around the neighboring Cu atom (U). The electronic properties of the plane depend on the relative magnitude of the kinetic energy (t) and the Coulomb repulsion (U). If U>>t, the electrons will not have enough energy to overcome the Coulomb repulsion and will remain localized around their respective Cu atom. This generates a "traffic jam of electrons"[**?**] usually referred to as

*In conventional BT, a single band has room for 2 electrons per unit cell. Any material with an odd number of electrons per unit cell (5 in this case) will have a partially-filled band and will therefore be metallic.

the "Mott state". Finally, note that the previous discussion leaves the spin as a variable degree of freedom. However, it can be proved using virtual hopping processes that the most favorable state is antiferromagnetic (see Fig. 2.1b).

The strong correlations of the Mott state make it very sensitive to changes in parameters like the doping (amount of extra charge carriers), the temperature or the biased current. Tuning these parameters gives rise to a wide variety of emergent phenomena that go well beyond the simple Mott state of the undoped parent compound. Fig. 2.2 shows the different electronic phases that arise when changing the (hole) doping of the parent compound. The microscopic origin of the different phases is still uncertain, however, it is clear that the strong correlations of the Mott state persist in the different phases[**?**]. We conclude this section by saying a few words on the different electronic phases in Fig. 2.2:

- The blue triangle-shaped region at low dopings is the antiferromagnetic state described by Mott and illustrated by Fig. 2.1b.

- The green region at intermediate dopings and low temperatures is frequently called the unconventional superconducting dome. Similar to conventional superconductivity, this electronic phase can be described by a single order parameter: the complex pseudowavefunction Ψ. However, in the unconventional superconducting phase Ψ has d-wave symmetry instead of the well-known s-symmetry encountered in conventional BCS theory. Furthermore, the size of the Cooper pairs (roughly given by the coherence length) and the superfluid density (indicative of the phase coherence) are both smaller than the ones of conventional superconductors.

- The yellow region spanned at intermediate dopings and high temperatures is usually called the pseudogap phase and it is characterized by a depletion of the electronic density of states at the Fermi energy[5].

- The purple funnel-shaped region at high doping levels and high temperatures receives the name of "Strange Metal phase". Transport properties in this region are fundamentally different from the ones of a canonical Fermi Liquid. For instance, the in-plane resistivity $\rho_{ab}(T)$ varies linearly with temperature and not quadratically as one would expect from Fermi Liquid Theory[6].

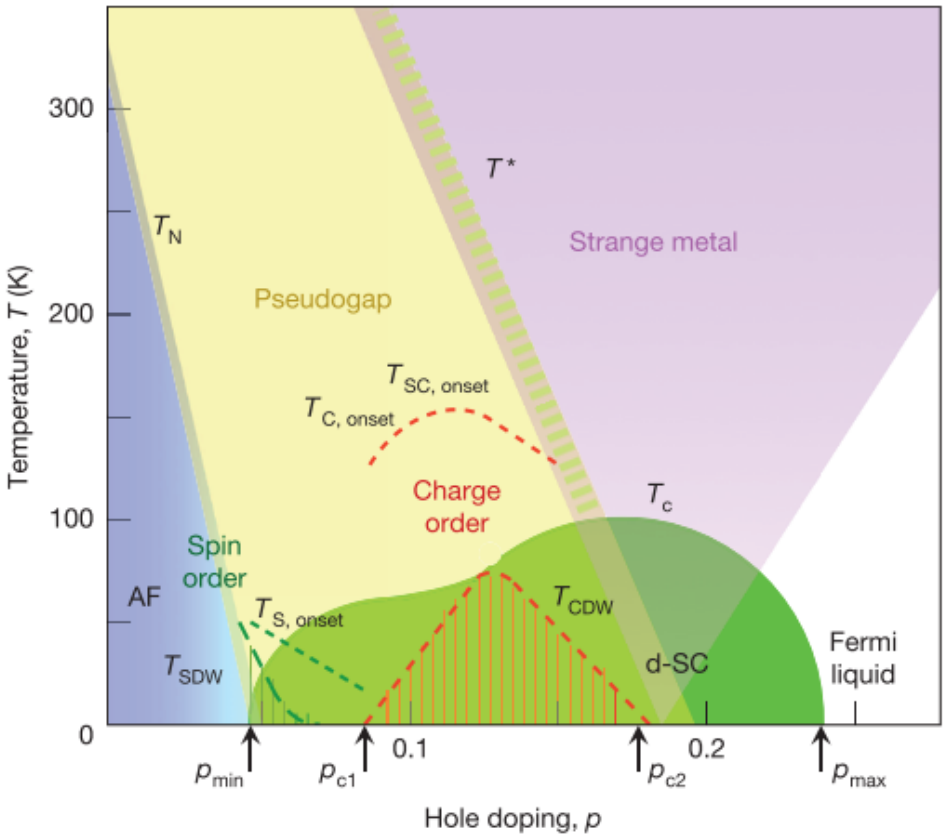

Figure 2.2: *Phase diagram of the copper oxides high temperature superconductors. Reprinted from Ref[**?**]*

- Finally, the white region at very high doping levels and intermediate temperatures can be described by the well known Fermi Liquid Theory.

2.2 STM : Exploring the Cuprates with a Conducting Tip

The different electronic phases shown in Fig. 2.2 are usually characterized by the presence of spatially inhomogeneous electronic features like the normal density of states or the superfluid density. Probing the local (topographic, transport, electronic) properties of the cuprates is therefore crucial to characterize the inhomogeneities and to get a better understanding of the different electronic phases.

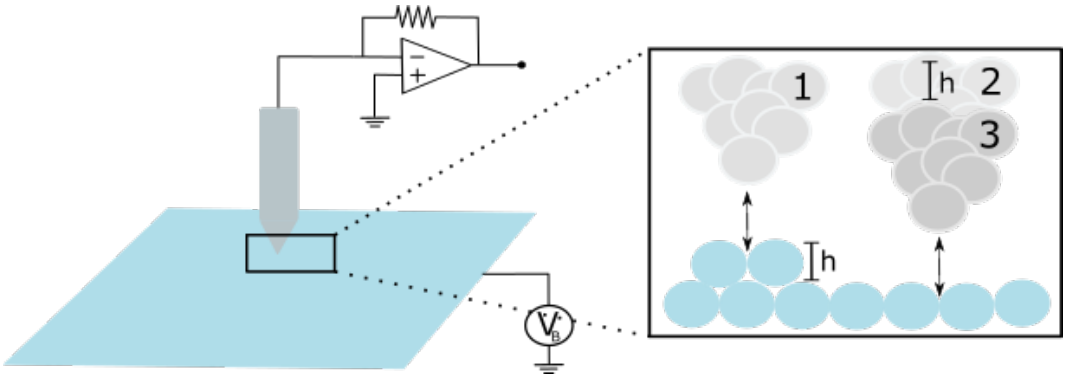

Figure 2.3: *Cartoon illustrating the basic principle behind STM. The circuit on top of the tip is a current amplifier and it is used to amplify the small tunneling current and convert it into volts so that it is easier to read. In order to obtain Vb volts between tip and sample, the tip can be grounded through the amplifier while Vb volts are applied to the sample.*

In this section we introduce the Scanning Tunneling Microscope, a local technique that has greatly contributed to our current understanding of the cuprates. The topographic and spectroscopic modes discussed in this chapter will set the ground for the techniques described in chapters 3 and 4.

Topography : Conventional STM

Scanning Tunneling Microscopy (STM) is one of the most valuable tools for probing topographic properties in condensed matter systems. The basic principle is illustrated in Fig. 2.3 : The application of a bias voltage between an atomically sharp tip, and a smooth conductive surface generates a net tunneling current that can be used to map the topography. The electrons tunnel through vacuum as if it was a simple 1D rectangular barrier, generating an exponentially dependent current on the tip-sample distance. The strong sensitivity of the current to the tip-sample distance can be used to map the topography of the sample.

In the constant current mode shown in Fig. 2.3 a feedback loop is used to keep the current constant whilst the tip scans the sample. After moving the tip to a new scan point($1 \rightarrow 2$), the feedback loop measures the new value of the current and adjusts the tip height to reach the setpoint value(3). The vertical adjustments of the tip can be recorded and identified with the topography of the sample.

Local Density of States : STS

Scanning Tunneling Spectroscopy (STS) is an operation mode of STM that allows to extract spectroscopic information on a local scale. The tunneling current between tip and sample contains not only information about the relative distance between them, but also regarding the density of electronic states of both of them. If the density of states at the tip is known, the local density of states below the tip $g_s(\epsilon)$ can be obtained for each scan point. The resulting dataset is usually called a spectroscopic map, and it is a 3-dimensional array containing the local density of states as a function of position and energy $g_s(x, y, \epsilon)$.

A detailed yet simple theoretical description of tunneling junctions was provided by Bardeen[9] and then adapted to the case of tip-sample tunneling in STM by Tersoff and Hamann[10]. This approach considers tip and sample as two separate sub-systems and calculates the amplitude of the electron transfer (tunneling matrix element) as the overlap of tip and sample eigenfunctions. Let $\chi_\nu(\mathbf{r})$ be a tip eigenfunction and $\psi_\mu(\mathbf{r})$ a sample eigenfunction, the tunneling matrix element is:

$$M_{\mu\nu} = \langle \chi_\nu | (H_S + H_{TR}) | \psi_\mu \rangle = \frac{\hbar^2}{2m} \int_{S_{TS}} \psi_\mu \nabla \chi_\nu^* - \chi_\nu^* \nabla \psi_\mu \, dr \tag{2.1}$$

where H_S and H_{TR} are the sample and transfer hamiltonians respectively, and the integral is performed at an arbitrary surface S_{TS} between tip and sample. The probability of an electron tunneling from a tip eigenstate χ_ν with energy $E_{T,\nu}$ to a sample eigenstate ψ_μ with energy $E_{S,\mu}$ is given by Fermi's Golden Rule :

$$P_{\chi_\nu \to \psi_\mu} = \frac{2\pi}{\hbar} |M_{\mu\nu}|^2 \delta(E_{S,\mu} - E_{T,\nu}). \tag{2.2}$$

Up to this point, we have calculated the probability of a single electron tunneling from a tip state χ_ν to a sample state ψ_μ. The corresponding current would be $I = e \cdot P_{\chi_\nu \to \psi_\mu}$. However, the tip and sample are characterized by a continuous set of eigenvalues, so we must sum over all of them to obtain the total current. Furthermore, at zero temperature the filled and empty states of a system are separated by a sharp Fermi surface at the fermi level whilst at finite temperatures, this sharp surface is smeared out according to the Fermi Dirac distribution. The number of filled states at finite temperature is therefore given by $f(E - E_f, T)^*$ and the number of

$^* f(E - E_f, T) = \dfrac{1}{1 + exp\left[(E - E_f)/(k_B T)\right]}$

empty states is given by $1 - f(E - E_f, T)$. Assuming a tip-sample voltage bias V_b and noting that an electron can only tunnel from an occupied state on the tip χ_ν to an empty state on the sample ψ_μ, we can write the total tunneling current that flows from tip to sample as:

$$I_{T\to S} = 2 \cdot \frac{2\pi e}{\hbar} \sum_{\mu\nu} f(E_\nu) \left[1 - f(E_\mu)\right] |M_{\mu\nu}|^2 \delta(E_{T,\nu} - E_{S,\mu} - eV_b) \tag{2.3}$$

where the factor 2 comes from the two different spin channels. In the same way, we can write the tunneling current flowing from sample to tip as:

$$I_{S\to T} = 2 \cdot \frac{2\pi e}{\hbar} \sum_{\mu\nu} f(E_\nu) \left[1 - f(E_\mu)\right] |M_{\nu\mu}|^2 \delta(E_{T,\mu} - E_{S,\nu} - eV_b). \tag{2.4}$$

Finally, we can substract both contributions and replace the sum over eigenstates by an integral over energies $\left(\sum_\mu \longrightarrow \int g(\epsilon) d\epsilon\right)$ to obtain the net tunneling current:

$$I = \frac{4\pi e}{\hbar} \int_{-\infty}^{\infty} |M|^2 \left[f(\epsilon - eV_b) - f(\epsilon)\right] g_s(\epsilon) g_t(\epsilon - eV_b) d\epsilon \tag{2.5}$$

where g_t and g_s are the tip and sample local density of states respectively. This expression can be further simplified by making two assumptions. If $k_B T$ is smaller than the energy resolution required (if g_s at the studied energy changes smoothly compared to $k_B T$) the Fermi-Dirac distributions can be approximated by step functions. Finally, the tip can be chosen so that its density of states around the Fermi level is almost constant, leading to:

$$I = \frac{4\pi e}{\hbar} g_t(0) \int_0^{eV_B} |M|^2 g_s(\epsilon)\, d\epsilon. \tag{2.6}$$

This expression shows that the tunneling current is proportional to the integrated density of states, furthermore, it implies that the differential conductance is proportional to the sample density of states:

$$dI/dV \propto g_s(\epsilon = eV). \tag{2.7}$$

In a typical STM-STS measurement, the so-called "sample and hold" algorithm is applied : the scanning is stopped at each point and the feedback loop is turned off in order to perform constant-height I vs V and a

dI/dV vs V curves. The differential conductance (dI/dV) can be calculated by using a lock-in amplifier to modulate dV and measure dI. In this way, we can calculate the density of states at a particular point as a function of energy. Repeating this measurement at each scan point will result on a spectroscopic map : $g_s(x, y, \epsilon)$.

2.3 Cuprates in Presence of a Transport Current

Establising a transport current into a copper oxide superconductor generally results in a change of its electronic properties. These current-induced electronic states have been studied in transport and Angle Resolved Photoemision (ARPES) experiments at low temperatures and several dopping levels [1–4, 11]. A summary of the different electronic phases found experimentally at low temperatures($\simeq 4.2K$) is shown in Fig. 2.4. Note that at zero current, Fig. 2.4 is in good agreement with the low-temperature regime of Fig. 2.2, however increasing the biased current results in several emergent electronic phases. The resistivity range associated with each phase is included in table 2.1.

As we saw in Fig. 2.1b, the antiferromagnetic (AF) Mott state of the cuprates is an insulator with virtually infinite resistance. This large resistance makes low-temperature experiments in presence of current challenging due to large heat dissipation. Although no experiments on cuprates have been reported in this regime, we found some literature where large pulsed currents were applied to the insulating Mott state of Ca_2RuO_4[11]. It was shown that the insulating gap characteristic of the Mott state closes under the presence of moderate current densities, giving rise to a finite-resistance diamagnetic state. Several mechanisms like the increase in the electron temperature or the reduction of electron correlations by the biased current have been proposed to explain the closing of the gap. However, experiments in this region have been proved to be extremely challenging due to large heat dissipation, and several articles have been retracted due to unnoticed heating issues [12][13].

The narrow pseudogap (PG) region located between the AF phase and the superconducting dome has not been studied in the presence of large current densities and therefore remains mysterious in this regime.

The d-wave superconducting dome (d-SC), characterized by a lack of electrical resistance expands over most of the dopping range at low temperatures and current densities. This region has been shown to evolve into a normal metallic state with finite resistance in the presence of large current densities. The transition to the normal state involves at least two

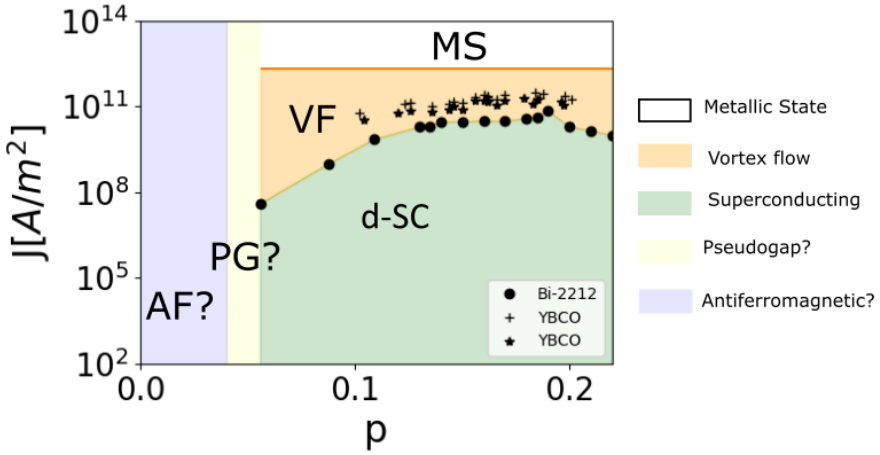

Figure 2.4: *Low-temperature ($\simeq$ 4.2K) phase diagram of cuprates in presence of a transport current constructed from experimental data in Refs [1–4, 11, 14]*

critical currents* : the depinning current density $j_{depinning}$ where vortex motion develops (maximum loss-free current), and the depairing current density $j_{depairing}$ where Cooper pairs dissociate. We will refer to the intermediate state between $j_{depinning}$ and $j_{depairing}$ as Vortex Flow (VF) regime for reasons that will soon become obvious.

A reasonable estimate of the depairing current density can be obtained using the Ginzburg-Landau theory[15]:

$$j_{depairing} = \frac{cH_c(T)}{3\sqrt{6}\pi\lambda(T)} = j_{(depairing,0)}\left(1 - \frac{T}{T_c}\right)^{3/2} \tag{2.8}$$

where $j_{(depairing,0)}$ is the depairing current at zero temperature, $\lambda(T)$ is the London penetration length and H_c is the thermodynamic critical field. Inserting typical values for $\lambda(0)$ and H_c[16] leads to $j_{(depairing,0)} = 3.3 \cdot 10^{12} A/m^2$, which is in good agreement with the results obtained using pulsed measurement techniques in YBCO films[17] [18]. We plot this value as an horizontal line in Fig. 2.4 to separate the "metallic state"(MS) where cooper pairs no longer exist† from the VF state.

Finding the depinning critical current $j_{depinning}$ is a bit more challenging. Brandt and Indenbom[20] obtained an expression (eq 3.25 in Ref [20])

*A third critical current defined as the critical current at which the superfluid stiffness vanishes has also been conjectured

†Preformed Cooper pairs have shown to exist in the disordered superconductor titanium nitride[19], so it is possible that they also exist in this current-induced metallic state.

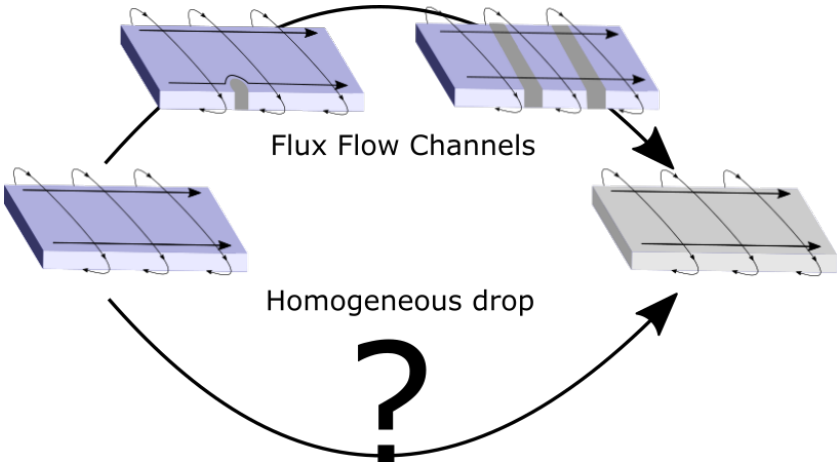

Figure 2.5: *Current-induced transition from a SC to a metallic state. The upper part shows a scenario where all the voltage of the intermediate VF state is dropped over a few flux-flow channels whilst most of the sample remains superconducting. The lower part of the figure indicated the possibility of a homogeneous drop of the voltage over the whole sample in the intermediate VF state.*

that allows to extract $j_{depinning}$ from the width of the hysteretic magnetization curve M(H) of a sample with known cross section. The crosses and stars in Fig. 2.4 correspond to $j_{(depinning,0)}$ obtained from such magnetization measurements in YBCO films from Refs.[2] and [14]. Alternatively, $j_{(depinning,0)}$ can be obtained from transport meassurements as the current density that generates a certain voltage over the sample. The circles in Fig. 2.4 correspond to the current densities that generated a voltage drop of $0.08[V/m]$ over the thin Bi-2212 samples of Ref.[1].

The intermediate state between the de-pairing and de-pinning critical currents, here denoted vortex flow regime (VF) is not completely understood. The biased current generates a magnetic field that penetrates the sample in form of quantized flux. In order to minimize energy, the flux lines arrange in a flux-line lattice (FLL) pinned to the defects of the sample. If the Lorentz force generated by the current at a vortex is greater than its pinning energy, it will start moving perpendicular to the current. The draft generated by the flow of these flux lines causes the resistive VF state. The voltage distribution $V(x,y)$ of this resistive VF state is controversial. Some groups suggest a scenario where most of the sample remains superconducting and the voltage induced by the current drops exclusively at a few vortex-flow channels, whilst other groups suggest a homogeneous drop of the voltage over the whole sample. Both possibilities are illustrated in Fig. 2.5.

The upper part of Fig. 2.5 shows the formation of vortex-flow channels. If the magnetic field generated by the current exceeds its critical value at the edge, a normal region forms. The supercurrent will try to avoid this normal region flowing around it. The new path taken by the supercurrent enhances the magnetic field at the normal region, making it propagate towards the middle of the film. The magnetic flux penetrating at opposite sides of the film has opposite signs. This generates a flux-flow channel where flux tubes of opposite sign nucleate at the two edges and travel toward the middle of the film, where they annihilate each other. These flux-flow channels have been directly observed in magneto-optical experiments[21], and indirectly in ARPES[3] or through the frequency spectrum of the generated voltage noise[22].

The lower part of Fig. 2.5 indicates the possibility of a homogeneous potential drop over the sample as suggested by Ref[4].

Table 2.1: *Resistivities of the different current-induced electronic phases in fig.2.4*

Phase	Sample	Resistivity[Ωm]	Ref
Antiferromagnetic (AF)	-	∞	-
Pseudogap * (PG)	$YBa_2Cu_3O_{6+\delta}$	10^{-5}	[23][24]
	$La_{2-x}Sr_xCuO_4$	$(0.1-10)\cdot 10^{-5}$	[23][24]
	$Bi_2Sr_2CaCu_2O_{8+x}$	10^{-5}	[25] [26]
	$Bi_2Sr_{2-x}La_xCuO_{6+\delta}$	$(0.1-10)\cdot 10^{-5}$	[27]
d-Superconducting (d-SC)	-	0	-
Vortex Flow (VF)	$Bi_2Sr_2CaCu_2O_y$	10^{-8} ($\simeq 10^{-5}$ per channel)	[3][4]
Metallic State (MS)	$Bi_2Sr_2CaCu_2O_y$	$> 10\cdot 10^{-5}$	†

*The resistivities in the PG phase are taken at low current densities($< 1A/m^2$). We will assume this values to remain constant at larger current densities.

†The large current densities required to access this phase difficult the measurement of the resistivity. We therefore assume a continious transition from the VF regime and take $\rho > 10\cdot 10^{-5}$ as an orientative value.

Chapter 3

STM in Presence of a Transport Current : Local Density of States

In the previous chapter, we introduced STS as a powerful tool to probe electronic properties on a local scale. Here, we extend this technique to study local electronic properties in presence of a biased transport current. The additional current I_s introduces a new variable in the spectroscopic map $g(x, y, \epsilon) \rightarrow g(x, y, \epsilon, I_s)$ allowing us to study the influence of the transport current on the local density of states. In this brief chapter, we discuss several spectroscopy experiments performed in the presence of a biased current on cuprates, and study how viable it is to reproduce them using STS.

3.1 Introduction

Scanning Tunneling Spectroscopic (STS) measurements in presence of a transport current can be implemented into any standard STM-STS setup just by including an extra contact to the sample. This extra contact allows to drive a current bias through the sample whilst performing a typical STM-STS experiment. If the sample is resistive, the biased current will induce a potential gradient over it. In the absence of additional feedback loops, the induced local potential $V(x, y)$ generates a small error in the topograph. However, since the change in local potential from point to point ($\simeq 1\mu V/nm$) is frequently much smaller than the biased voltage ($\simeq 100mV$) this error can be safely neglected.

The forced current will also modify the local density of states $g(x, y, \epsilon, I_s)$ obtained in STS. For metallic samples, large current densities ($10^{10} A/m^2$)

can lead to deviations in Ohm's law around 1%[28]. However, for superconducting samples a large enough current density can drive a phase transition into a normal metallic state[29] (see Fig. 2.4). The microscopic mechanisms that cause the breakdown of superconductivity are well established in conventional superconductors, however, they are not yet fully understood in unconventional superconductors[**?**]. The local resolution of non-equilibrium STS seems like a formidable tool to shed some light on such microscopic processes. Furthermore, studying the effect of large currents in more exotic electronic phases like the pseudogap phase can help us to understand its nature.

3.2 State of the Art : Spectroscopy in Presence of a Transport Current

Spectroscopy in presence of a transport current on conventional superconductors was firstly addressed experimentally by C. D. Mitescu et al. In a more detailed study, Anthore et al[30] used a small fixed tunnel junction to prove that the effect of large current densities ($\simeq 2 \times 10^{10} A/m^2$) on the electronic spectra of aluminum is similar to the one caused by large magnetic fields (i.e., the closing of the gap and the widening of coherence peaks). The weakening of pair-correlations caused by the large current densities (or fields) will eventually result in a metallic normal state identical to the one obtained at high temperatures.

In high-temperature superconductors, the normal state reached after forcing large current densities seems to be different from the one obtained at large temperatures ($T > T_C$) or magnetic fields ($B > B_C$). Angle-Resolved Photoemision Spectroscopy (ARPES) results show a gapped fermi surface above Tc without well-defined quasiparticles[31]. In contrast, transport measurements under large magnetic fields show quantum oscillations, implying the existence of a Fermi surface and therefore a more conventional FL-behavour[32]. Recent ARPES studies point towards a third normal state accessed at large current densities. We conclude this section by reviewing two of such studies performed on $Bi_2Sr_2CaCu_2O_{8+x}$, the preferred cuprate for surface-sensitive measurements.

Kaminski et al[4] observed the broadening and disappearing of the coherence peaks on the ARPES spectra performed at the VF region (orange in Fig. 2.4). They attributed this loss of single-particle coherence to the phase slips associated with flux motion. In this scenario, phase fluctuations along the whole sample destroy the single-particle coherence and

the voltage drops homogeneously over the whole sample. See the lower part of Fig. 2.5.

Naamneh et al[3] also studied the VF region, however they found an energy split on the ARPES spectra with no notable broadening of the peaks. The split of the spectra corresponded to the voltage dropped over the sample. This scenario suggests that most of the sample remains free of phase fluctuations, and all the voltage drops in a few narrow vortex-flow channels. Since the vortex flow channels are small compared to the size of the sample, most of the emitted electrons come from superconducting regions at different chemical potentials, giving a split on the spectra whilst maintaining single-particle coherence. This scenario is in agreement with the flux-flow channels shown in the upper part of Fig. 2.5.

3.3 Viability of STS in Presence of a Transport Current on Cuprates

The above-described spectroscopy experiments in presence of a transport current lack spatial resolution. They either focus on the local properties at a particular point of the sample or on the spectroscopic properties of its whole surface. Furthermore, all of them were performed in the vortex-flow region (orange in Fig. 2.4).

Scanning Tunneling Spectroscopy in presence of a transport current could give access to the local density of states (LDOS) of the different current-induced phases in Fig. 2.4. Since changes in the LDOS are expected when approaching a phase transition, we discuss the current density required to induce the four possible phase transitions and the viability to observe them using STM in presence of a transport current.

Experimentally, the different electronic phases at zero current (AF, PG, SC) can be accessed by annealing the sample in an Oxygen or inert environment (control of the hole content by inserting/removing O_2 in the buffer layers). The current-induced states ususally require large current densities, so thin samples are frequently required to minimize heat losses.

Antiferromagnetic Phase $\rightarrow$?

The fully antiferromagnetic phase is completely insulating and therefore will give zero tunneling current at low temperatures (4.2 K). Increasing the temperature of the measurement could thermally activate the charge carriers generating a small tunneling current and revealing the gap of this

phase. As it was already discussed, the large resistivity of the AF phase makes measurements in presence of a transport current challenging due to heat dissipation. Runing short ($1\mu s$) pulses will certainly help to reduce heat dissipation. Although the current induced ($j \simeq 1A/m^2$) gap supression in the Mott state of Ca_2RuO_4 [11] could point towards a similar state in cuprates, the serious heating issues encountered [12][13] are not too optimistic.

Pseudogap Phase $\rightarrow$?

The lack of experimental data of the pseudogap phase in presence of a large current densities could be attributed to the difficulty of reaching the precise dopping level. The annealing temperatures needed to access the pseudogap phase are frequently high in macroscopic samples. However, the larger surface/volume ratio of thin films reduces the required annealing temperature. The dissipated power in this region due to the flow of the current should be able to run moderate current densities without major loses. For these reasons we belive that despite the lack of prior experiments, performing STS in this region should be possible. However, the required current density to observe a change in the LDOS is uncertain and should be found experimentally.

Superconducting $\rightarrow$ Vortex Flow

The vortex-flow state (orange in Fig. 2.4) spans the region between the de-pinning critical current and the de-pairing critical current at intermediate dopings. Observing the change in the spectroscopic maps as the depinning critical current is approached is probably the easiest experiment since it only requires moderate current densities ($\simeq 10^8$) in underdoped samples ($p \simeq 0.05$), and it the existence a phase transition is well established. Limiting the current to a reasonable value of $10mA$ to prevent heat issues, and chosing an underdoped sample would require a cross section of roughly $10^2 A/m^2$ (see table 3.1).

Once the current density is increased above the depinning value, the resistive Flux Flow regime is entered. Performing non-eq STS in this phase will help us to directly confirm if the induced voltage drops homogeneously through the sample, or if it drops in a few vortex-flow channels perpendicular to the current (see Fig. 2.5).

In the case of a homogeneous voltage drop, a homogeneous broadening of the coherence peaks is expected in the whole field of view. Other-

wise, if the voltage drops exclusively at a few narrow channels whilst the rest of the sample remains superconducting, sharp coherence peaks are expected in most of the sample and the closing of the gap should be seen in the channels. The width of the channels is around $1\mu m$ and therefore accessible within the large field of view of STM ($1.5\mu m$).

Vortex Flow $\rightarrow$ Metallic State

It is unsure if the current-induced metallic phase reached when surpassing the depairing current (white on Fig. 2.4) corresponds to the Strange Metal phase (purple region in Fig. 2.2) that has long puzzeled theorists. Although spectroscopic experimetns in this region are certainly interesting, the exceptional large current required to brake the Cooper pairs make them challenging. In order of achieve the deparing current ($j_{depairing} \simeq 10^{12} A/m^2$) with a reasonable current of 10mA, the cross section of the sample must not be larger than $10^{-2}\mu m^2$. This would mean a thickness of $1nm$ for a flake of $10\mu m$ width. These dimensions are only viable in monolayered thin samples.

Table 3.1: *Estimate current densities required to induce several phase transitions. The value of σ conrresponds to the required cross section to achieve the current density on the left limiting the total current to 10 mA.*

Phase Transition	$j_[A/m^2]$	$\sigma[\mu m^2]$
Superconducting $\rightarrow$ Vortex Flow	$\simeq 10^8$	10^2
Vortex Flow $\rightarrow$ Metallic	3.3×10^{12} *	0.3×10^{-2}
Pseudogap $\rightarrow$?	?	?
Antiferromagnetic $\rightarrow$?	$\simeq 10^5$ †	$\simeq 10^5$

*Underdopped side of the green dome in Fig. 2.4

†Note that this value does only give an estimate of a possible phase transition, since these kind of transitions have only been observed on Ca_2RuO_4 so far

Chapter 4

STM in Presence of a Transport Current : Local Potential

In the previous chapter, the viability of scanning tunneling spectroscopic meassurements in pressence of a transport current was studied. If the sample is in a resistive state, the biased current will generate a potential drop $V(x,y)$ over it. Such a potential map can be accessed from the spectroscopic information in a technique that is frequently called Scanning Tunneling Potentiometry (STP). In this chapter, we will review this technique and its several implementations to conclude studying its viability on cuprates.

4.1 Introduction : STP

Figure 4.1 illustrates the simple interrupted feedback STP implementation developed by Kirtley and coworkers based on the "sample and hold" alorithm used in STS. In addition to the tip-sample voltage bias, a current bias is applied along the sample generating a local potential $V(x,y)$ on its surface. The gray dotted line gives a visual reference to apply Kirchhoff's voltage law to the loop:

$$V_b + V(x,y) = I_t \cdot R_{junction} + I_t \cdot R_{tip} \tag{4.1}$$

where $R_{junction}$ and R_{tip} are the tunneling junction and tip resistances, and I_t is the tunneling current. The local potential at a precise point $V(x,y)$ can now be identified with the voltage bias that makes the tunneling current zero:

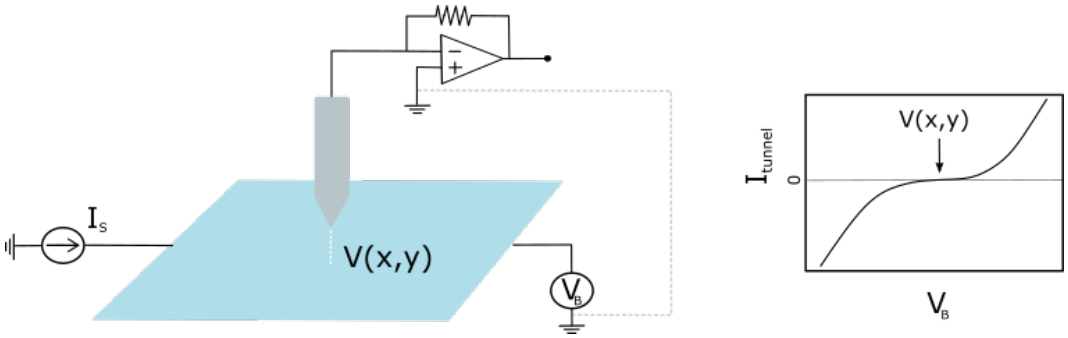

Figure 4.1: *Cartoon illustrating the basic principle behind STP. Voltage bias (V_b) and sample bias (I_s) are both applied to the sample while the tip performs STM-STS measurements. The local potential ($V(x,y)$) generated by the current bias at a particular point can be identified with the voltage V_B such that $I(V_B) = 0$. In practice, the current source can be replaced by a large voltage source and a large resistor in series. The gray line guides the eye for Kirchhoff's voltage law*

$$I_t = 0 \rightarrow V_b + V(x,y) = 0 \rightarrow V(x,y) = -V_b \tag{4.2}$$

Equation 4.2 is the foundation of the interrupted feedback STP and allows us to extract $V(x,y)$ at each point from the spectroscopic information. The voltage that zeroes the current can be obtained from the intercept of the I vs V curve with the I = 0 axis (see Fig. 4.1). Note that this technique must be modified when working with gapped samples since the tunneling current will be zero for all the energies within the gap. In this case, the condition $I_t = 0$ must be replaced by $I_t = I_{setpoint}$, increasing the sensibility to tip-sample vibrations.

The above described STP implementation (interrupted feedback) is the easiest to execute in an STM-STS setup. Other implementations like the AC+DC feedback or the noise potentiometry need additional feedback and integrating circuits that frequently precise fine-tuning.

The spatial resolution of an STP experiment can be defined as the smallest distance (Δx) over which a variation in local potential ΔV can be detected:

$$\Delta x = \Delta V / E = \Delta V / \rho j \tag{4.3}$$

where E is the electrinc field on the sample, ρ is the resistivity, j is the biased current density and ΔV is the voltage resolution (smallest variation in V that our setup can detect). Note that we used ohms law $E = \rho j$ assuming an homogeneous drop of the potential over the sample. For this reason, equation 4.3 provides a good definition of the spatial resolution in

metallic samples, and a lower bond to the resolution in inhomogeneous samples.

In order to detect the induced voltage drop, the spatial resolution Δx must be small compared to the field of view of the STM measurement which is only limited by the extension of the piezos ($< 1.5\mu m$ in our case). We must therefore minimize the voltage resolution ΔV of the setup whilst maximizing the current and the resistivity of the sample. We devote the remaining of this section to study how to minimize the voltage resolution ΔV of our present setup, and leave the maximization of ρ and j for the next section, where experiments on different samples are discussed.

The voltage resolution of a setup can effectively be identified with the noise in the voltage measurement. The main sources of noise in STM are : the $1/f$ flicker noise intrinsic to all electronic devices, the mechanical instability of the tip-sample junction, the thermal (Johnson) noise, the shot noise, and the electronic drifts.

The condition 4.1 makes the voltage measurement robust against mechanical instability since no voltage drops between tip and sample when determining $V(x, y)$. Furthermore, since no tunneling current is present, shot noise should also be absent. The $1/f$ pink noise is unavoidable in the kHz bandwidth of conventional STM*, but could be reduced at higher frequencies. Finally, the thermal noise provides a fundamental limit to the voltage resolution:

$$\Delta V \geq 4K_b TR \tag{4.4}$$

where K_b is the boltzman constant, T is the temperature and R is the junction's resistance. For a typical $G\Omega$ junction at liquid helium temperature (4.2 K) Eq 4.4 gives a fundamental noise limit of $0.5\mu V/\sqrt{Hz}$.

Preliminary measurements with our setup show a noise level of $0.8mV$, which is almost 3 orders of magnitude higher than the fundamental limit when less than a second is spent on each pixel. This excess of noise can be attributed to several causes. Firstly, the large duration of the measurement might result in overall drifts in our electronics. Additionally, a bad electrical contact to our sample could cause the biased current to generate large temperature fluctuations that will result in a large Flicker noise. Sample heating also results in different tip and sample fermi distributions generating an undesired thermovoltage between them. Ref[33] showed that it is possible to eliminate this thermovoltage contribution by simple mathematical operations on different voltage maps.

*The large impedance of the junction together with the capacitance of the coax cable behave a low-pass filter limiting conventional STM signals to small frequencies ($\simeq kHz$)

4.2 State of the Art : Previous STP Experiments

In the last section, we saw that the voltage resolution ΔV is only dependent on the setup, whilst the spatial resolution Δx is determined by the used sample through

$$\Delta x = \frac{\Delta V}{\rho j} \tag{4.5}$$

where $\Delta V \geq 4K_bTR\Delta f$, ρ is the resistivity of the studied sample, and j is the biased current density. The small spatial resolution required for our experiments can be achieved using highly resistive samples and large current bias densities. In practice, the sample must be conductive enough to allow the flow of a tunneling current, and the transport current must be low enough to prevent Joule heating ($P \propto I^2R$) at low temperatures. These limitations reduce the number of suitable samples for STP experiments.

Thin (few nm) gold films are frequently used to demonstrate the technique or to report improvements on the voltage resolution[34–36] due to their easy availability and predictive behavior. The $Si(111) - \sqrt{3}x\sqrt{3} - Ag$ surface, formed by depositing one layer of Ag atoms on a Si surface has also been widely studied by STP[37–40] due to the controversy surrounding its atomic arrangement, surface state, and transport properties. More recently, the availability of low-cost and good quality monolayer and few-layer graphene has made it a great candidate for STP studies[33, 41–43].

Equation 4.5 can be used to plot the contours of constant spatial resolution for a setup of voltage resolution ΔV. Figure 4.2 shows three of such contour plots ($\Delta x = 5nm$, $\Delta x = 50nm$ and $\Delta x = 500nm$) in log-log scale for our particular setup ($\Delta V = 0.8mV$). We also include in the plot several experiments in the literature as points at particulat j and ρ. An experiment lying on the $\Delta x = 50nm$ line has a voltage drop of $0.8mV$ over $50nm$. An experiment located above the $\Delta x = 50nm$ line would have a potential drop greater than $0.8mV$ per $50nm$.

Most of the studied experiments in Fig. 4.2 lie above the $\Delta x = 500nm$ line and would therefore develop a voltage drop greater than $0.8mV$ over $500nm$. Therefore, using a large field of view ($\simeq 1.5\mu m$) would allow us to detect a voltage drop in most of the experiments with our current voltage resolution ($0.8mV$). Note however that a spatial resolution of $500nm$ is almost two orders of magnitude larger than the spatial resolution of a conventional topograph. Therefore, if a correlation with topographic features ($\simeq$ few nm) is desired, higher current densities are needed.

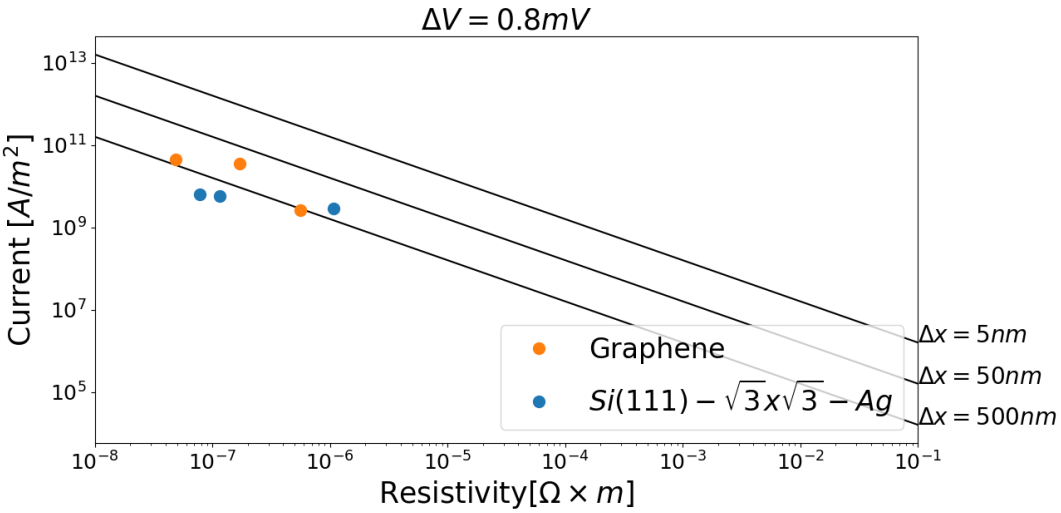

Figure 4.2: *Constant spatial resolution curves in logarithmic scale for our present setup($\Delta V = 0.8mV$) and values for the estimated biased current densities and resistivities of different STP experiments on graphene (Refs. [33, 42, 43]) and $Si(111)\sqrt{3}\sqrt{3} - Ag$ (Refs. [38–40]). The current densities were obtained assuming the sheets to be atomically flat.*

4.3 Viability of STP on Cuprates

Some studies were also performed on cuprates during the early days of STP. In 1989 Kent et al took a potential and topograph map of a YBCO thin film above the critical temperature[44], correlating structural deffects with higher normal-state resistivity regions. A few years later the same group extended the data to low temperatures[35]. A thin ($9.8nm$) Gold film was deposited on top of a thin YBCO film so that below the critical temperature all the bias current is carried by the gold layer, whilst above the critical temperature the bias current flows through both, gold and YBCO films. At the critical temperature (85 K), they observed a drop in the local potential at a change in the topography. The interpretation of these results was not clear and remained somewhat opened. After suggesting several possible artifacts, the possibility of a normal-state dupple on the superconducting sample is also mentioned. No structure was found below the superconducting temperature.

The discussed early works showed the potential of STP to characterize phase transitions. However, the usage of a top gold layer at low temperatures decreased the spatial resolution of the technique and did not allow

spectroscopic measurements. In the following, we re-discuss the viability of STP to directly probe the current induced electronic phases of the cuprates at low temperatures.

Figure 4.3 is identical to Fig. 4.2 but instead of plotting experiments performed on Graphene or $Si(111) - \sqrt{3}x\sqrt{3} - Ag$, several ARPES experiments on $Bi_2Sr_2CaCu_2O_{8+x}$ are included. The different shaded regions represent the distinct electronic phases and are obtained by combining the information in Fig. 2.2 and table 2.1.

The intersection of the shaded regions with the $\Delta x = 50nm$ line gives the current density needed to produce a voltage drop of $0.8mV$ over $50nm$, that can be safely detected in a field of view of $1.5\mu m$ with our $0.8mV$ voltage resolution. The value of this current for each phase, referred to as $j_{min}(\Delta x = 50nm)$ is shown in table 4.1. In practice, the cryogenic environment limits the total current through the wires to $\simeq 10mA$. For this reason, we also include in table 4.1 the cross-section σ_{max} needed to achieve $j_{min}(\Delta x = 50nm)$ with a current of $10mA$.

Note that the antiferromagnetic and superconducting phases are not included in this diagram. As we discussed in the previous chapter, the large restivity of the antiferromagnetic region makes heat diffipation a major issue. On the other hand, the zero resistance superconducting state does not generate a potential distribution when when a current is applied and therefore is not suitable for potentiometric studies. To conclude this chapter, we discuss the viability of STP on the remaining regions of Fig. 4.3.

Vortex Flow State (VF)

The vortex flow region is indicated with two orange rectangles in Fig. 4.3. The left rectangle, labeled homogeneous, is constructed using different resistivities found in Bi-2212 experiments and assuming them to be constant over the whole sample. This corresponds to the homogeneous scenario discussed in chapter 2, and illustrated in Fig. 2.5. The minimum current needed to produce a voltage drop of $0.8mV$ over $50nm$ (j_{min}) is indicated by a black square in Fig. 4.3, and printed in table4.1. Restricting the current to 10mA leads to a cross-section of roughly $\sigma_{min} \simeq 100nm \times 1\mu m$, falling into the thin-film regime.

The right orange rectangle assumes that the voltage is dropped on a few flux-flow channels, and indicates the expected resistivities of one of such flux channels (see the upper part of Fig. 2.5). Following Ref[3], it was assumed that there is approximately 1 flux-flow channel of $1\mu m$ width

every 150 μm. Since all the voltage is dropped in a few flux-flow channels, each of the channels has a large resistivity as compared to the homogeneous case, locating this region to the right of the homogeneous VF regime. The required current to achieve $\Delta x = 50nm$ is smaller than in the homogeneous scenario, making the experiment less demanding an leading to a maximum cross section of roughly $1\mu m \times 10\mu m$ that also falls into the thin-film/flake regime.

Pseudogap State (PG)

The yellow PG region was constructed using the typical low current resistivity values shown in table2.1 and assuming them to remain constant for larger current densities. In this case, the value of j_{min} decreases to $1.6 \cdot 10^8 A/m^2$ increasing σ_{max} to roughly $1\mu m \cdot 50\mu m$. Smaller cross-sections will give larger current densities for the same current, and therefore increase the spatial resolution of STP beyond $50nm$. STP experiments in this region can be particularly interesting to understand the hydrodynamics in the PG phase.

Metallic State (MS)

The large resistivities and current densities required to access the metallic region make it ideal for potentiometric studies. We can see that the expected region for experiments in the metallic phase (white in Fig. 4.3) is located way above the $\Delta x = 5nm$ line, indicating subnanometer resolution in STP studies. As we mentioned in the previous chapter, the large current densities required to reach the metallic state can only be achieved in mono/few layered samples ($\sigma_{max} \simeq 1\mu m \times 1nm$).

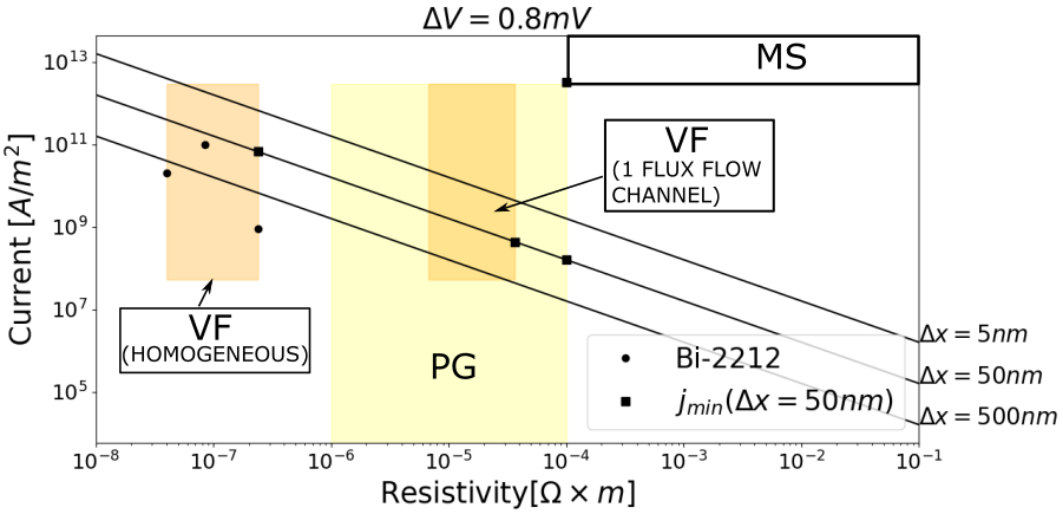

Figure 4.3: *Constant spatial resolution curves in logarithmic scale for our present setup($\Delta V = 0.8mV$) and values (Resistivity, Current) of different ARPES experiments on Bi-2212 in the VF phase (Refs. [1, 3, 4]). The shaded regions indicate the different resistivities for the phases in Fig. 2.4, and their intersection with the constant resolution lines give j_{min} ($50nm$) - defined as the minimum current needed to generate a voltage drop of $0.8mV$ over $50nm$*

Table 4.1: *Current density needed to produce a voltage drop of* $0.8mV$ *over* $50nm$ $j_{min}(\Delta x = 50nm)$ *in the different electronic phases. We also include the cross-section* σ_{max} *required to reach* $j_{min}(\Delta x = 50nm)$ *using a current of* $10mA$.

Phase	$j_{min}(\Delta x = 50nm)[A/m^2]$	$\sigma_{max}[\mu m^2]$
Vortex Flow (single channel)	4.3×10^8	2.3×10^1
Vortex Flow (homogeneous)	6.7×10^{10}	1.4×10^{-1}
Pseudogap	1.6×10^8	6.2×10^1
Metallic State	3.3×10^{12}	3×10^{-3}

Chapter 5

Towards Sample Fabrication

In this chapter, we describe the first steps towards the realization of the experiments described in chapters 3 and 4. After considering the demanding sample requirements imposed by the experiments, we decide to use thin Bi-2212 flakes due to their small cross-sections and easy doping control. We then develop a simple fabrication method that allows contacting and in-situ cleaving of the thin flakes. After performing some tests on this method we conclude that although viable, it has shown to be surprisingly complicated. Although we believe that the presented method should not yet be abandoned, we suggest more elaborate methods involving standard lithography.

5.1 Sample requirements

This brief section is devoted to select a sample that meets the strong requirements for STM experiments in presence of a transport current discussed in chapters 3 and 4

Selecting the Crystal

So far, we have studied the universal properties of the cuprates arising from their common building block: the CuO_2 plane. However, factors like the precise chemical composition of the buffer layers or the number of CuO_2 planes per unit cell provide each crystal with particular and distinctive properties.

Bismuth cuprates ($Bi_2Sr_2Ca_{n-1}Cu_nO_{2n+4+x}$) are frequently the preferred crystal for surface-sensitive measurements like STM or ARPES. In particu-

lar, the one with two CuO_2 planes per unit cell ($Bi_2Sr_2CaCu_2O_{8+x}$, abbreviated Bi-2212) shown in Fig. 5.2 has several characteristics that make it ideal for these experiments. Unlike other cuprates like YBCCO, the oxygen content (doping) of Bi-2212 is stable at room temperature and the bonds between the BiO layers that connect the unit cells in the z-direction are weak, causing the parent compound to be easily cleaved.

In contrast to other crystals like $YBa_2Cu_3O_{7-\delta}$ or Sr_2RhO_4, the annealing temperature required to access the pseudogap phase in bulk Bi-2212 is remarkably high. This large annealing temperature makes it challenging to access the pseudogap phase in macroscopic crystals without damaging them. Fortunately, the large surface to volume ratio of thinner Bi-2212 samples gives access to the whole dopping range, including the PG[45].

The weak intralayer bond, together with the wide doping range available and the small cross-section of Bi-2212 thin samples makes them a great candidate for our experiments. We will focus the rest of this thesis on Bi-2212 thin films. However, other macroscopic crystals like Sr_2RhO_4 could be suitable for studying the pseudogap region in presence of a current without making use of thin samples.

In situ Cleaving

The high surface sensitivity of the techniques described in chapters 3 and 4 requires clean, inert and atomically flat surfaces. Ideally, the crystal could be grown and transferred into the measuring chamber without breaking the UHV. In practice, UHV growing systems attached to measuring devices like ARPES or STM are not usual. Alternatively, the sample can be cleaved in-situ to expose a clean flat surface. The simplicity of cleaving as compared to in situ growth makes it the preferred method, and in situ cleaving of bulk crystals are performed routinely in ARPES or STM setups.

In the standard in-situ cleaving method, the macroscopic crystal is glued to a sample holder, whilst a ceramic post ($d \simeq 2mm$) is glued to the other side of the crystal. The post can be removed in situ by exerting a force on it, thereby cleaving the crystal. This method has been proved to work on either large macroscopic samples or Molecular-beam epitaxy (MBE) grown thin films with large surface and good interaction with the substrate. Exfoliated samples are frequently too small to attach a post. Furthermore, the interaction of the exfoliated flakes with the substrate is generally not too strong leading to a removal of the whole sample from the substrate instead of cleaving (see Fig. 5.3). Although in-situ cleaving of exfoliated flakes was proven to be challenging, we gave the first steps towards a sim-

ple cleaving method.

Dimensions and Contacting of the Crystal

A macroscopic Bi-2212 crystal has typical dimensions of $5mm \times 5mm \times 1mm$. A regular indium rod of $0.25mm$ diameter could be connected to the side of the crystal to force the transport current. After the in-situ cleaving this would lead to a cross-section of roughly $\sigma \simeq 0.25mm \times 5mm$, and biasing $10mA$ will result in a current density of $8 \times 10^3 A/m^2$ which is roughly 4 orders of magnitude lower than the depinning current density required to observe a change on the LDOS (see table 3.1) or the current density required to obtain the local potential $V(x, y)$ in the vortex flow region with a spatial resolution of $\Delta x = 50nm$ (see table 4.1).

In order to obtain large current densities, we could benefit from the asymmetry of the c-axis resistivity of the cuprates. Since $\rho_c/\rho ab \simeq 10^3$ for underdoped cuprates at low temperatures[46], if two rods are connected to the top surface (not to the side) of a macroscopic crystal, most of the current will flow through the uppermost CuO_2 plane leading to remarkably large current densities whilst keeping the overall current low (see Fig. 5.1). Conventional cleaving methods remove the uppermost layers of the sample, therefore, if the contacts are placed exclusively on the top surface of the sample, they will also be removed. Alternative cleaving methods involving the structuring of the crystal could be used to surpass this difficulty. However, we did not pursue this approach.

The most extended way of reaching large current densities at low temperatures without major heat losses is simply reducing the size of the sample. Thinner samples can achieve large current densities even when contacted from the side (not from the top). The layered structure of Bi-2212 makes it easy to obtain thin flakes using a simple exfoliation method. The typical cross-sections obtained by exfoliation are $\sigma \simeq 100nm \times 100\mu m = 10\mu m^2$, which is thin enough to detect changes in the LDOS (see table 3.1) and even to resolve the local induced potential $V(x, y)$ in the pseudogap or in the vortex flow regime with a spatial resolution of $\Delta x = 50nm$ (see table 4.1). For this reason, we will focus the rest of this thesis on cleaving thin Bi-2212 flakes.

5.2 Fabrication Method

As it was briefly discussed, the common cleaving method where a ceramic post glued to the sample and then ripped off is only suitable for either

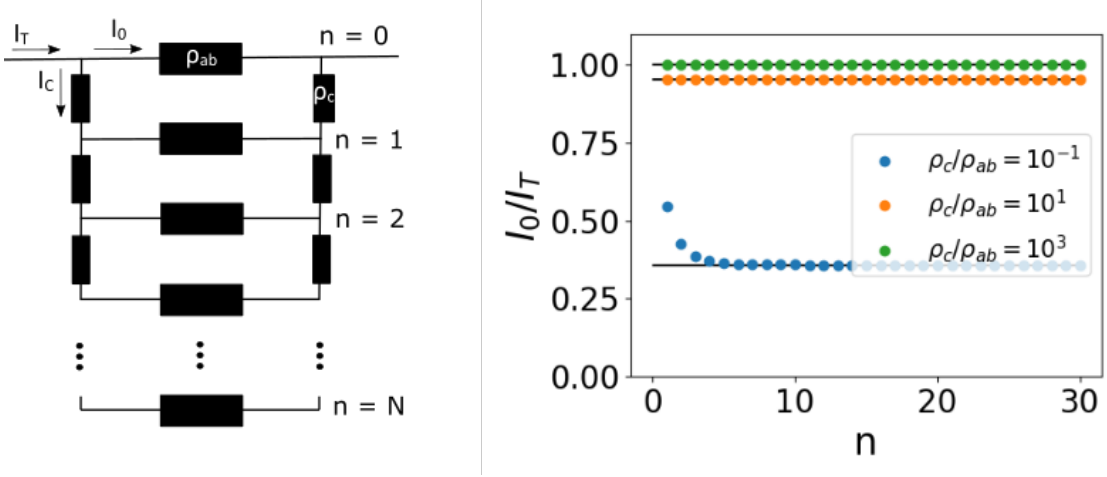

Figure 5.1: *Resistor network simulation of a layered material contacted from the top. The normalized current flowing through the uppermost layer is plotted as a function of the number of layers for different ratios of c axis and in plane resistance. In underdopped Bi-2212 the ratio is* $\rho_c/\rho ab \simeq 10^3$ *and therefore almost all the current (99%) flows through the uppermost layer when contacted from the top.*

macroscopic samples or MBE-grown thin films with a large surface and strong adhesion to the substrate. In this section, we present an alternative method that could be used to cleave exfoliated thin Bi-2212 flakes in-situ.

Method

The unit cell of Bi-2212 is depicted in the inset of Fig. 5.2.-a). Spanning this unit cell in the 'x' and 'y' directions results in a monolayer of Bi-2212, and stacking several monolayers in the 'z' direction gives the macroscopic crystal. The weak Van der Waals interaction between layers makes macroscopic Bi-2212 crystals easy to exfoliate. The Scotch tape method [47] uses a piece of tape to repeatedly peel off layers of the crystal by folding the tape into itself.

Performing the Scotch tape exfoliation with 2 or 3 peelings results in thin crystals that can be transferred into a UHV compatible Kapton tape (Fig. 5.2.-b). A good optical system and a couple of micromanipulators can now be used to select a parent flake and place it on top of a cleaned substrate with pre-patterned contacts (Fig. 5.2.-c). Finally, the chip with the stuck Kapton tape can be inserted into the preparation chamber of the STM, and the exfoliation can be performed in situ at UHV using a wobble

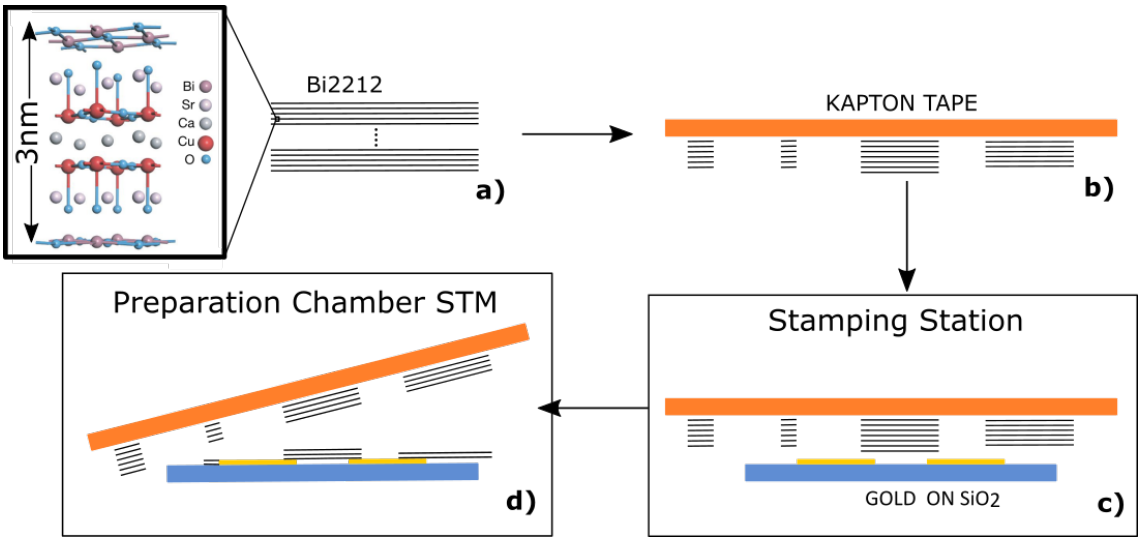

Figure 5.2: *Sample fabrication. A macroscopic crystal* ***a)*** *is exfoliated into kapton tape using the scoth tape method* ***b)*** *and it is stuck into a clean Si/SiO_2 chip with prepatterned contacts* ***c)*** *using an stamping station. Finally, the kapton tape can be removed inside the STM chamber* ***d)*** *cleaving the flakes and exposing a clean surface.*

stick to remove the tape containing the parent flake (5.2.-d).

Challenges

There are two considerations that will determine the efficiency of the above-described method: choosing a suitable parent flake and maximizing the interaction between the parent flake and the substrate.

Fig. 5.3 gives a closer look into the cleaving process. In order to cleave the crystal, the tape-crystal interaction and the substrate-crystal interactions must be greater than the Van der Waals interaction between the layers of the crystal. Note that this Van Der Waals coupling between layers is not homogeneous among the z-direction, but changes depending on the concentration of impurities (symbolized by a star in Fig. 5.3). A weak tape-layer interaction (compared to the intralayer VdW interaction) results in the Bi-2212 being transferred instead of cleaved, whilst a weak substrate-layer interaction prevents the Bi-2212 from sticking to the substrate. The tape-crystal interaction is usually strong. However maximizing the interaction between Bi-2212 and substrate (either Gold or SiO_2) is one of the main challenges of this method.

The dimensions and flatness of the parent flake will also play an im-

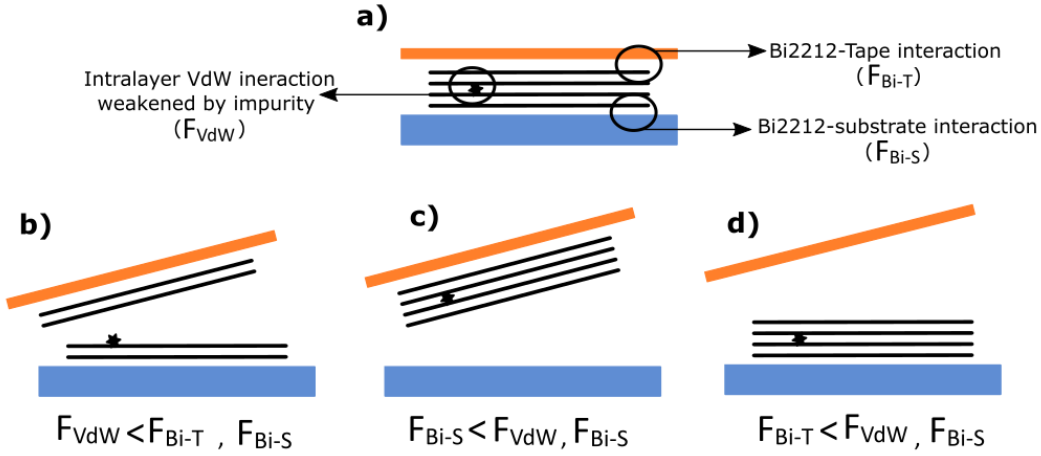

Figure 5.3: *Main interactions involved in the cleaving process. The relative value between the magnitudes of the forces will determine if the sample cleaves* ***(a)****, stays on the tape* ***(b)*** *or is completely transferred* ***(c)*** *to the substrate*

portant role in the cleaving process. Thicker flakes are more likely to have a large concentration of impurities in a particular region, locally decreasing the VdW force and making cleaving easier. For this reason, cleaving of thin films poses a severe challenge, whilst cleaving of thicker crystals is performed on a daily basis by STM and ARPES groups. Similar reasoning applies to parent flakes with different surface areas. In addition, the initial parent flake is not monoatomically flat as shown in Fig. 5.2 and Fig. 5.3, but usually consists of several terraces of different thicknesses. This leads to an inhomogeneous contact with the substrate that can cause the fragmentation of the parent flake after cleaving.

In the rest of this chapter, we will try to surpass the mentioned challenges by maximizing the interaction between Bi-2212 and the substrate (Si/SiO_2 or gold) and selecting an adequate parent flake so that the cleaving is optimal.

5.3 Cleaving Bi-2212 onto Si/SiO_2

The preferred substrate for thin film deposition or cleaving is frequently silicon dioxide (Si/SiO_2). Its optical properties allow to easily identify thin films and even determine their thickness using reflectometry or optical microscopy techniques. Furthermore, the surface of SiO_2 can be chemically activated in order to enhance its interaction with a deposited sample.

In this section, we study the cleaving process of Bi-2212 onto a SiO_2 substrate as depicted in Fig. 5.3. We will focus on selecting the ideal parent flake and enhancing its interaction with the substrate so that the cleaving is optimal. The additional annealing step (2 minutes at 100C$^\circ$) between the sticking of the Kapton containing the parent flake onto the substrate (Fig. 5.2**-c)**) and its removal (Fig. 5.2**-d)**) introduced by Ref. [48] is also adapted in all the experiments. Once the cleaving process is optimized, we examine the resulting cleaved flakes and study the evolution of their interaction with the substrate.

Maximizing the Interaction between Bi-2212 and Si/SiO_2

The surface of $SiO2$ can be chemically activated in order to increase its reactivity and enhance the interaction with the deposited sample. Dry surface activation can be achieved by means of O_2 plasma inside a Reactive Ion Etcher (RIE): the oxygen ions bombard the SiO_2 removing all the adsorbents and producing hydroxyl groups (-OH) on the surface. The generated silanol (Si-O-H) terminations make the silica surface reactive to electrostatic or hydrogen bonding. Adequate control over the surface activation process will help us to maximize the interaction between the SiO_2 and the Bi-2212 flake.

The precise RIE parameters that maximize the surface functionalization are dependent on the particular geometry and conditions of the employed etcher. However, there is a certain regime where most of the references [49–51] seem to agree (see table 5.1). Guided by the experiment, we observe that the most relevant parameter of the process is the etching time. For this reason, we set the RF power, oxygen flow, and pressure of the process constant* and carefully examine the effect of the etching time.

In order to quantify the effect of the etching time on the cleaving process, we define the cleaving yield of a particular flake "j" as the ratio between the area of the parent flake and the area of the different cleaved flakes that result from exfoliating the parent flake onto the substrate :

$$Yield_j = \frac{\text{Area of the parent flake}_j}{\sum_i \text{Area of cleaved flake}_i}. \tag{5.1}$$

The defined cleaving yield can be calculated from the optical images of the parent and cleaved flakes as indicated in appendix A.

*The values of these parameters (RF power, oxygen flow, and pressure) were chosen based on the advice of colleagues that use the same RIE machine for similar purposes.

Table 5.1: *Relevant parameters of the Reactive Ion etching process. The optimal parameters are specific of the particular RIE machine used. We include the typical values from Refs. [49–51]*

Parameter	Typical values	Used value
RF power[W]	50-100	100
Pressure[mtorr]	15-40	30
Etching time[s]	10 - 240	120
Oxygen Flow[sscm]	10-60	50

Finding the cleaving yield of several flakes with the same RIE parameters gives us an idea of the effectiveness of the cleaving process. Finally, comparing the cleaving yields for different etching times can help us to obtain the optimal value. Figure 5.4 shows the average cleaving yield obtained for two flakes when using different etching times. The dimensions of the parent flakes used for this study were all large (surface area $\simeq 8 \times 10^5 \mu m^2$) in an attempt to ease comparison. We attribute the behavior shown in 5.4 to the creation of hydroxyl groups on the surface of the substrate until a saturation point is reached and the plasma starts destroying the bonds. In any case, etching times around 120 seconds seem to be optimal for the cleaving.

Selecting a Suitable Parent Flake

The flakes used to discuss the effect of the etching time were all intentionally large (surface $\simeq 8 \times 10^5 \mu m^2$) for practical purposes. However, in the course of the experiment, we realized that smaller flakes lead to higher cleaving yields. Here, we use the optimized RIE parameters in table 5.1 to study the effect that the surface area of the parent flake has on the cleaving yield.

Figure 5.5 shows the cleaving yields for 20 parent flakes with different surface areas. Flakes of different sizes can be obtained after contin-

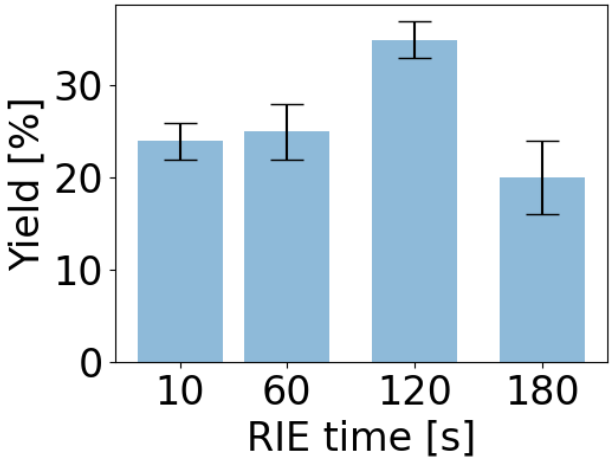

Figure 5.4: *Average (2 parent flakes of similar area $\simeq 8 \times 10^5 \mu m^2$) cleaving yield for different etching times. The optimized etching time of 120 will be used for the rest of the experiments.*

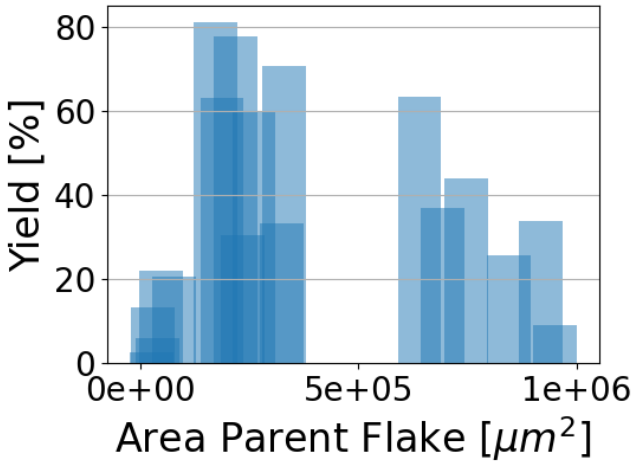

Figure 5.5: *Cleaving yield of 20 different flakes of variable surface area. A maximum in the cleaving yield is found for parent flakes with surface area around $2 \times 10^5 \mu m^2$. The large surface region located in the right of the x-axis is the one we used to study the influence of the etching time (see Fig. 5.4).*

uously peeling off the crystals using the Scotch tape method. For this reason, smaller flakes will not only have a smaller surface but will also be thinner. Note also that this will not lead to a homogeneous set of initial parent flakes, explaining the empty region between $4 \times 10^5 \mu m^2$ and $6 \times 10^5 \mu m^2$. The maximum around $2 \times 10^5 \mu m^2$ seems to point towards a "sweet spot" of maximum interaction where cleaving yields as large as 80% are achieved. Note that this optimized cleaving yield is almost double the one obtained for either larger or smaller flakes. We argue that smaller flakes are tougher to cleave due to lower concentration of impurities, whilst larger flakes fracture easier leading to lower yields.

Fragmentation and Thickness Distribution of the Cleaved Flakes

In the previous sections, we talked about the cleaving yield without specifying if the original parent flake resulted in a unique cleaved flake, or if it resulted in several different flakes of distinct sizes and thicknesses. Here we give a closer look into such cleaved flakes. We use parent flakes that lie in the "sweet spot" of Fig. 5.5 and functionalize the Si/SiO_2 substrates using the values in table 5.1.

Figure 5.6**-a)** shows the cleaved flakes resulting from exfoliating a parent flake located in the "sweet spot" of Fig. 5.5 onto a Si/SiO_2 substrate. Using the software "Image J", the intensity of each flake can be used to generate a mask (Fig. 5.6**-b)**) that allows obtaining the area and mean contrast of every flake (see appendix A). Although the multivalued function relating thickness and contrast (Fig. A.3 in appendix A) does not allow to unambiguously identify the thickness of a flake with its contrast, it can be quickly measured using a profilometer.

Figure 5.6**-c)** shows the percentage of the initial parent flake that was cleaved onto the different flakes of 5.6**-b)**. Overall, almost 69% of the original parent flake was effectively cleaved. However, this 69% was distributed among 7 different flakes that we label in Fig. 5.6**-b)**. Flakes 1, 5, and 6 have inhomogeneous thicknesses that range from $3nm$ to $5nm$ corresponding to monolayer and bilayer sheets. Together these 3 flakes cover roughly the 15% of the initial parent flake ($12264 \mu m^2$) which is a remarkable large value for mono(bi) layer flakes. The small flakes labeled with numbers 4 and 7 seem to be connected by an underlying monolayer and have thicknesses of tens of nanometers, representing only the 5% of the area of the initial parent flake. There is also a 10% of the initial parent flake that resulted in a group of various overlapping flakes with thickness

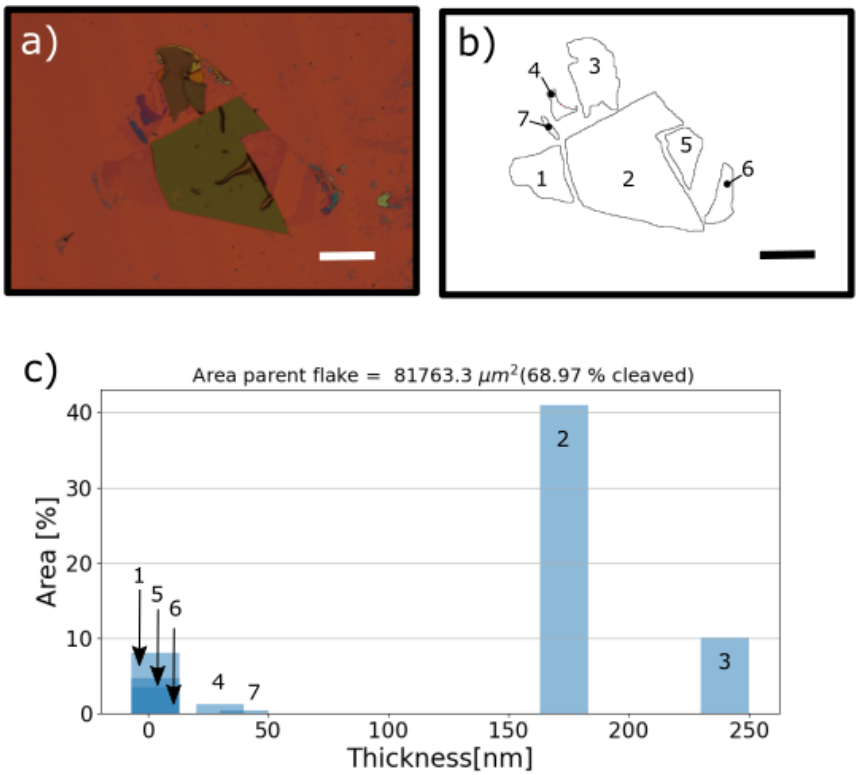

Figure 5.6: *Flake distribution of an optimal-cleaved flake.**a-)** Original optical microscope image, **b-)** generated masks for flake identification, **c-)** thickness distribution of the cleaved flakes as measured with the profilometer. The white/black scale corresponds to* $200\mu m$.

around $250nm$. Finally, the remaining 40% comes from a single flake of $170nm$ thickness labeled with the number 2. It is interesting to note that this large flake (2) seems to be on top of flakes the thinnest flakes (1, 5, and 6) and connected to flake 3.

From the above discussion, it follows that the studied parent flake could be stamped onto a substrate and that once the tape is peeled off the substrate, the 40% of the parent flake will be cleaved onto a single homogeneous flake exposing a clean surface. Therefore, if we deposit two thin and narrow electrodes on the substrate as shown in Fig. 5.10a, and assume the cleaving onto Gold to be similar to the one onto Si/SiO_2, there is a large probability that the big flake lands on both electrodes.

However, the distribution of cleaved flakes is not always as favorable as the one shown in Fig. 5.6. Figure 5.7 shows the same experiment repeated for six different parent flakes of similar sizes*, all of them lying in the "sweet spot" of Fig. 5.5. On top of the optical image, we include the generated mask for each parent flake. Although the total cleaving yield of all the flakes is high ($> 65\%$), they all show fragmentation into several flakes of different thicknesses. However, most of the samples still contain at least one large cleaved flake. Furthermore, some of the cleaved flakes seem to overlap, and an underlying monolayer film connects most of the flakes. For instance, sample e) shows exclusively this monolayer sheet with several few-layered flakes on top. If all the cleaved flakes were indeed connected (either by percolation or by an underlying monolayer sheet like the one shown in Fig. 5.7-e)), exfoliating the parent flake onto a chip with pre-patterned electrodes would result in a set of flakes electrically connected either by percolation or by an underlying mono/few layers. This somewhat optimistic scenario would be great for our purposes since it will result in a current through the flakes as long as the parent flake is stamped on top of the contacts.

In definitive, the large cleaving yields shown in Fig. 5.5 and Fig. 5.7 seem like a great step towards our cleaving method (Fig. 5.2). However, we found two further challenges that prevented us from implementing the full method in a real chip: **(1)**The time-degrading of the Bi-2212/SiO_2 interaction, and **(2)** the low cleaving yields found when exfoliating flakes onto gold. We devote the rest of this chapter to discuss these two effects and propose solutions for them.

*flakes a and b in Fig. 5.7 come from the same "grandparent flake"

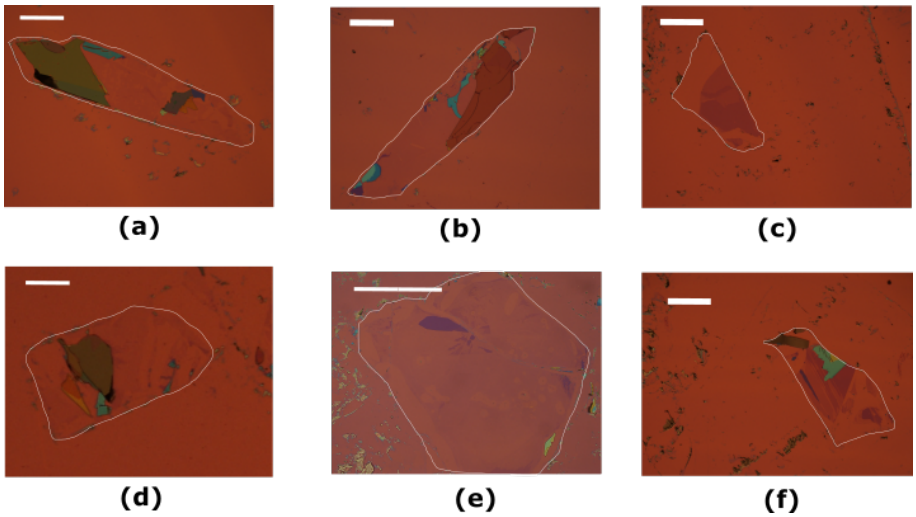

Figure 5.7: *Resulting flakes after exfoliating 6 different parent flakes of similar sizes into clean Si/SiO_2 substrates. The scale bar corresponds to $200\mu m$. Most of the samples resulted on at least one large homogeneous flake.*

Time Degrading of the Interaction between Bi-2212 and Si/SiO_2

The optimized cleaving yield of roughly 70% shown in Fig. 5.5 seems promising for our in-situ cleaving method. However, in a realistic scenario, the Kapton tape will be removed inside the STM, and therefore some time will pass between the stamping of the Kapton tape (Fig. 5.2-c) and its removal (Fig. 5.2-d). First attempts on in-situ cleaving inside the STM seemed to point towards the degrading of the interaction between Bi-2212 and SiO_2 with time.

Figure 5.8 shows the evolution of the cleaving yield as a function of the time between stamping and removal of the tape containing the parent flake. Three flakes were averaged to find the cleaving yield for each time. The significant decrease on the cleaving yield in the timescale of an hour was attributed to the degrading of the interaction between flake and substrate over time.

In order to prevent the degrading of the interaction with time, the sample could be kept in an inert environment at all times. For example, an Argon box could be used to transport the sample from the stamping station to the STM. We hope that an inert environment prevents the degrading of the interaction between substrate and flake, ensuring the original cleaving yields ($\simeq$ 70%).

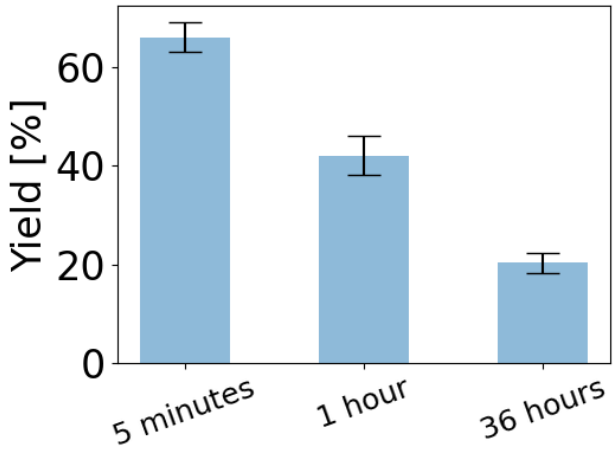

Figure 5.8: *Time degrading of the Bi-2212 to SiO_2 bond for parent flakes located at the "sweet spot" of Fig. 5.5. The cleaving yield at each degrading time was calculated using 3 different parent flakes.*

5.4 Cleaving Bi-2212 onto Gold

Although the stamped flake will mainly be in contact with Si/SiO_2 in our fabrication method, good interaction with the gold electrodes is also important to minimize contact resistance and ensure adequate cleaving. We choose Gold electrodes based on the low contact resistance with Bi-2212 flakes that they have shown in transport measurements [25]. In addition, DFT calculations supported by experimental data showed that the interaction between Gold and a wide variety of VdW materials is frequently greater than the intralayer VdW forces, making it ideal for cleaving [52]. However, our preliminary attempts of cleaving Bi-2212 onto Gold were far from successful.

Figure 5.9-a) shows an example of a cleaved Bi-2212 flake onto a gold substrate that was cleaned using the RIE parameters shown in table 5.1 and where the additional heating step (2mins, 100C°) between stamping and cleaving of the parent flake was applied. The cleaving yield is almost 0%. This remarkably low yield could be attributed to the roughness of the surface, and to the aging of Gold on air. Ref [53] showed that cleaving yields close to 0% were obtained once the Gold substrate was exposed more than 15 minutes to air. We assume this is the main cause for our low yields

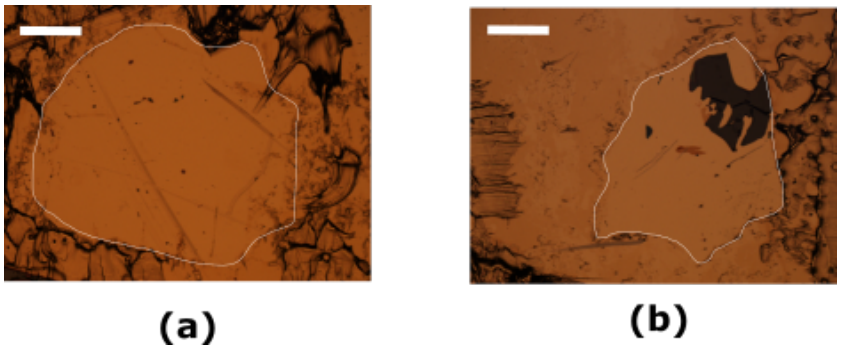

Figure 5.9: *Exfoliation of a parent flake into a Gold substrate* ***a)*** *using the same conditions than for* Si/SiO_2 *and* ***b)*** *removing the heating step and applying moderate pressure before peeling off the tape containing the parent flake. The white contours correspond to the area of the parent flake and were obtained as described in Appendix A.*

since all of our experiments were done at least one day after the Gold was deposited. However, we observed that the substitution of the heating step by the application of moderate pressure increased the yield to almost 15% (see Fig. 5.9-b) and Fig. 5.10b) even if the gold substrate was exposed to air for several days.

The unexpected low cleaving yield found when exfoliating Bi-2212 onto Gold, suggests minimizing the amount of gold in our prefabricated chips (see Fig. 5.10a) as well as exposing the gold electrodes as briefly as possible to air after deposition.

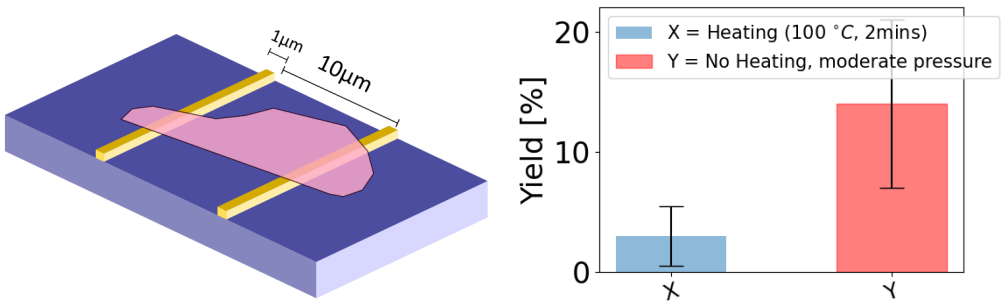

(a) ***(b)***

Figure 5.10: *Proposed design for the chip* ***(a)*** *given the low cleaving yields of Bi-2212 flakes onto gold* ***(b)****. The blue color bar (X) in* ***(b)*** *corresponds to the cleaving yield of Bi-2212 flakes onto gold obtained when using the optimized parameters found for cleaving onto* Si/SiO_2*. The red color bar (Y) in* ***(b)*** *corresponds to the same experiment substuting the heating step by the application of moderate pressure. The cleaving yields for* ***(b)*** *where obtained averaging 3 flakes for each experiment.*

Chapter 6

Summary and Outlook

Cuprates are among the best known strongly correlated materials. The strong correlation between electrons results in a wide variety of electronic phases that cannot be explained using the well-known Fermi Liquid theory. In this thesis, we outlined the first steps towards the local characterization of the current-induced electronic phases in cuprates using low-temperature Scanning Tunneling Microscopy (STM).

The first chapter gives an experimentalist's introduction to the world of strongly correlated systems. After discussing the presence of strong correlations in the parent compound, we introduce the doping-temperature phase diagram to discuss the several emergent phases. We then introduce Scanning Tunneling Microscopy (STM) and Scanning Tunneling Spectroscopy (STS) as powerful tools to locally probe these electronic phases. We conclude the chapter by constructing a doping-current phase diagram based on experimental data that will serve us as a map to explore the viability of our experiments on the different current-induced phases.

Chapters 3 and 4 introduce STM in presence of a transport current as a formidable tool to probe the local density of states (LDOS) and the local potential (V(x,y)) of the current-induced phases in cuprates. After discussing some relevant literature, we conclude that the Vortex-Flow and the Pseudogap phases are the most suitable phases for both experiments. Although the current densities required to observe a change in the LDOS ($\simeq 10^8 A/m^2$) are lower than the ones needed to observe a change in the local potential ($\simeq 10^{9-10} A/m^2$), both of the experiments require large current densities that suggest the usage of thin samples.

The final chapter studies the in-situ cleaving of thin Bi-2212 flakes required to perform the experiments discussed in chapters 3 and 4 on a clean surface. We present a simple method where a piece of tape containing a

parent flake is stamped onto a Si/SiO_2 chip with pre-patterned gold contacts and cleaved in-situ by removing the stamping tape. We maximized the cleaving yield by functionalizing the substrate using RIE and carefully selecting the parent flake. Although the optimized cleaving yield onto Si/SiO_2 was as high as 80%, we found two unexpected obstacles that complicate the implementation of the proposed method: **(1)** the degrading of the Bi-2212/SiO_2 interaction with time, and **(2)** the low cleaving yields ($\simeq$ 0%) onto Gold. We suggest that **(1)** the substrate with the stamped flake is kept in an inert environment until the tape is removed and the flake cleaved, and **(2)** that the gold surface on the chip is minimized and exposed to air as briefly as possible after deposited.

Perhaps the first check that must be performed before further elaborating or discarding the presented method consists of patterning thin and narrow gold electrodes onto a Si/SiO_2 substrate and checking how is the cleaving yield affected by the presence of the electrodes. Alternatively, more elaborated fabrication techniques like optical lithography could be used to secure the flake into the substrate or to structure it into a geometry that locally minimizes the VdW bonds allowing to easily cleave the flake.

Chapter 7

Acknowledgements

The work here reported would not have been possible without the hard work and bright ideas of a lot of people. I would like to thank all the members of Milan Allan's group for useful discussions and for creating an awesome and challenging work environment. In particular, I would like to thank Tjerk Benschop for his general guidance on the thesis and for being a great example of a passionate scientist. I would also like to thank Xing Chen for introducing me to the world of cleaving, and for always being accessible to discuss my ideas and questions. In addition, I would like to express my gratitude to Douwe Scholma and Thomas Mechielsen for their help and patience regarding all the technical issues involving etching, sputtering and clean room work.

Finally, I would like to thank my family and friends in Madrid and Leiden that kept me happy and motivated all the time.

Bibliography

[1] M. Naamneh, J. C. Campuzano, and A. Kanigel, *Doping dependence of the critical current in Bi2 Sr2 CaCu2 O8+δ*, Physical Review B - Condensed Matter and Materials Physics **90** (2014).

[2] S. H. Naqib and R. S. Islam, *Possible quantum critical behavior revealed by the critical current density of hole doped high-T c cuprates in comparison to heavy fermion superconductors*, Scientific Reports **9**, 1 (2019).

[3] M. Naamneh, J. C. Campuzano, and A. Kanigel, *The electronic structure of BSCCO in the presence of a super-current: Flux-flow, Doppler shift and quasiparticle pockets*, page 1 (2016).

[4] A. Kaminski, S. Rosenkranz, M. R. Norman, M. Randeria, Z. Z. Li, H. Raffy, and J. C. Campuzano, *Destroying coherence in high-temperature superconductors with current flow*, Physical Review X **6**, 1 (2016).

[5] A. A. Kordyuk, *Pseudogap from ARPES experiment: Three gaps in cuprates and topological superconductivity*, Low Temperature Physics **41**, 319 (2015).

[6] N. E. Hussey, H. Gordon-Moys, J. Kokalj, and R. H. McKenzie, *Generic strange-metal behaviour of overdoped cuprates*, Journal of Physics: Conference Series **449** (2013).

[7] B. Keimer, S. A. Kivelson, M. R. Norman, S. Uchida, and J. Zaanen, *From quantum matter to high-temperature superconductivity in copper oxides*, Nature **518**, 179 (2015).

[8] R. A. Davison, K. Schalm, and J. Zaanen, *Holographic duality and the resistivity of strange metals*, Physical Review B - Condensed Matter and Materials Physics **89**, 1 (2014).

[9] J. Bardeen, *Tunneling from a many-body point of view*, Physical Review Letters **6**, 57 (1961).

[10] R. J. Harvey, *Theory and Application for the Scanning Tunneling Microscope*, Physical Review Letters **50** (1983).

[11] R. Okazaki, Y. Nishina, Y. Yasui, F. Nakamura, T. Suzuki, and I. Terasaki, *Current-induced gap suppression in the mott insulator Ca 2RuO4*, Journal of the Physical Society of Japan **82**, 1 (2013).

[12] G. Mattoni, S. Yonezawa, and Y. Maeno, *Diamagnetic-like response from localised heating of a paramagnetic material*, arXiv **04570**, 1 (2020).

[13] C. Sow, R. Numasaki, G. Mattoni, S. Yonezawa, N. Kikugawa, S. Uji, and Y. Maeno, *In situ control of diamagnetism by electric current in Ca3 (Ru1-xTix)2 O7*, Physical Review Letters **122** (2019).

[14] S. H. Naqib and A. Semwal, *Low-temperature critical current of Y1-xCaxBa 2Cu3O7-δ thin films as a function of hole content and oxygen deficiency*, Physica C: Superconductivity and its Applications **425**, 14 (2005).

[15] M. Tinkham, *Introduction to Superconductivity*, in *2d ed*, pages 145–173, 1996.

[16] U. Welp, W. K. Kwok, G. W. Crabtree, K. G. Vandervoort, and J. Z. Liu, *Magnetic measurements of the upper critical field of YBa2Cu3O7- single crystals*, Physical Review Letters **62**, 1908 (1989).

[17] W. Lang, I. Puica, K. Siraj, M. Peruzzi, J. D. Pedarnig, and D. Bäuerle, *Critical current enhancement in YBa2Cu3O7-δ towards the intrinsic depairing value in short current pulses*, Physica C: Superconductivity and its Applications **460-462 II**, 827 (2007).

[18] M. N. Kunchur, D. K. Christen, C. E. Klabunde, and J. M. Phillips, *Pair-breaking effect of high current densities on the superconducting transition in YBa2Cu3O7-*, Physical Review Letters **72**, 752 (1994).

[19] K. M. Bastiaans, D. Chatzopoulos, J.-F. Ge, D. Cho, W. O. Tromp, J. M. van Ruitenbeek, M. H. Fischer, P. J. de Visser, D. J. Thoen,

E. F. C. Driessen, T. M. Klapwijk, and M. P. Allan, *Direct evidence for Cooper pairing without a spectral gap in a disordered superconductor above T_{C}*, (2021).

[20] E. H. Brandt and M. Indenbom, *Type-II-superconductor strip with current in a perpendicular magnetic field*, Physical Review B **48**, 12893 (1993).

[21] R. P. Huebener, *Dynamics of magnetic flux structures in superconductors*, Physics Reports **13**, 143 (1974).

[22] G. Churilov, V. Dmitriev, and A. Beskorsyi, *Generation of High-frequency Oscillations by Thin Superconducting Tin Films*, Soviet Journal of Experimental and Theoretical Physics Letters **10**, 146 (1969).

[23] N. Barisic, M. K. Chan, Y. Li, G. Yu, X. Zhao, M. Dressel, A. Smontara, and M. Greven, *Universal sheet resistance and revised phase diagram of the cuprate high-temperature superconductors*, Proceedings of the National Academy of Sciences of the United States of America **110**, 12235 (2013).

[24] Y. Ando, S. Komiya, K. Segawa, S. Ono, and Y. Kurita, *Electronic phase diagram of high-Tc, cuprate superconductors from a mapping of the In-plane resistivity curvature*, Physical Review Letters **93**, 1 (2004).

[25] E. Sterpetti, J. Biscaras, A. Erb, and A. Shukla, *Comprehensive phase diagram of two-dimensional space charge doped Bi2Sr2CaCu2O8+x*, Nature Communications **8** (2017).

[26] Y. Yamada, T. Watanabe, and M. Suzuki, *Fabrication and transport properties for cleaved thin film BSCCO single crystals*, IEEE Transactions on Applied Superconductivity **17**, 3533 (2007).

[27] S. Ono and Y. Ando, *Evolution of the resistivity anisotropy in (formula presented) single crystals for a wide range of hole doping*, Physical Review B - Condensed Matter and Materials Physics **67**, 9 (2003).

[28] P. W. Bridgman, *The Failure of Ohm ' s Law in Gold and Silver at High Current Densities*, Proceedings of the American Academy of Arts and Sciences **57**, 131 (1922).

[29] Y. Seo, Y. Qin, K. Choi, and J. Yoon, *Current-induced suppression of superconductivity in tantalum thin films at zero magnetic field*, eprint arXiv:cond-mat/0504340 (2005).

[30] A. Anthore, H. Pothier, and D. Esteve, *Density of States in a Superconductor Carrying a Supercurrent*, Physical Review Letters **90**, 4 (2003).

[31] A. Kanigel, U. Chatterjee, M. Randeria, M. R. Norman, G. Koren, K. Kadowaki, and J. C. Campuzano, *Evidence for pairing above the transition temperature of cuprate superconductors from the electronic dispersion in the pseudogap phase*, Physical Review Letters **101** (2008).

[32] N. Doiron-Leyraud, C. Proust, D. LeBoeuf, J. Levallois, J. B. Bonnemaison, R. Liang, D. A. Bonn, W. N. Hardy, and L. Taillefer, *Quantum oscillations and the Fermi surface in an underdoped high-T c superconductor*, Nature **447**, 565 (2007).

[33] P. Willke, T. Druga, R. G. Ulbrich, M. A. Schneider, and M. Wenderoth, *Spatial extent of a Landauer residual-resistivity dipole in graphene quantified by scanning tunnelling potentiometry*, Nature Communications **6**, 1 (2015).

[34] M. Rozler and M. R. Beasley, *Design and performance of a practical variable-temperature scanning tunneling potentiometry system*, Review of Scientific Instruments **79** (2008).

[35] A. D. Kent, I. Maggio Aprile, P. Niedermann, C. Renner, and O. Fischer, *Scanning tunneling potentiometry studies of Y 1 Ba 2 Cu 3 O 7 x and gold thin films*, Journal of Vacuum Science & Technology A: Vacuum, Surfaces, and Films **8**, 459 (1990).

[36] M. Hamada and Y. Hasegawa, *Development of scanning tunneling potentiometry for semiconducting samples*, Japanese Journal of Applied Physics **51** (2012).

[37] T. Druga, M. Wenderoth, J. Homoth, M. A. Schneider, and R. G. Ulbrich, *A versatile high resolution scanning tunneling potentiometry implementation*, Review of Scientific Instruments **81** (2010).

[38] J. Homoth, M. Wenderoth, T. Druga, L. Winking, R. G. Ulbrich, C. A. Bobisch, B. Weyers, A. Bannani, E. Zubkov, A. M. Bernhart, M. R. Kaspers, and R. Möller, *Electronic transport on the nanoscale: Ballistic transmission and Ohm's law*, Nano Letters **9**, 1588 (2009).

[39] A. Bannani, C. A. Bobisch, and R. Möller, *Local potentiometry using a multiprobe scanning tunneling microscope*, Review of Scientific Instruments **79** (2008).

[40] F. Lüpke, S. Korte, V. Cherepanov, and B. Voigtländer, *Scanning tunneling potentiometry implemented into a multi-tip setup by software*, Review of Scientific Instruments **86**, 1 (2015).

[41] W. Wang, K. Munakata, M. Rozler, and M. R. Beasley, *Local transport measurements at mesoscopic length scales using scanning tunneling potentiometry*, Physical Review Letters **110** (2013).

[42] P. Willke, T. Kotzott, T. Pruschke, and M. Wenderoth, *Magnetotransport on the nano scale*, Nature Communications **8**, 1 (2017).

[43] A. Sinterhauf, G. A. Traeger, D. Momeni Pakdehi, P. Schädlich, P. Willke, F. Speck, T. Seyller, C. Tegenkamp, K. Pierz, H. W. Schumacher, and M. Wenderoth, *Substrate induced nanoscale resistance variation in epitaxial graphene*, Nature Communications **11**, 1 (2020).

[44] A. D. Kent, I. Maggio Aprile, P. Niedermann, and A. Fischer, *Direct measurements of the effects of inhomogeneities on the normal-state transport properties of YBa2Cu3O7x thin films*, Physical Review B **39**, 12363 (1989).

[45] U. Chatterjee, M. Shi, D. Ai, J. Zhao, A. Kanigel, S. Rosenkranz, H. Raffy, Z. Z. Li, K. Kadowaki, D. G. Hinks, Z. J. Xu, J. S. Wen, G. Gu, C. T. Lin, H. Claus, M. R. Norman, M. Randeria, and J. C. Campuzano, *Observation of a D-wave nodal liquid in highly underdoped Bi 2 Sr 2 CaCu 2 O 8+δ*, Nature Physics **6**, 99 (2010).

[46] A. Mourachkine, *High-Temperature Superconductivity in Cuprates: The Nonlinear Mechanism and Tunneling Measurements*, Springer US, 2010.

[47] I. V. G. K. S. Novoselov, A. K. Geim, S. V. Morozov, D. Jiang, Y. Zhang, S. V. Dubonos and A. A. Firsov, *Electric Field Effect in Atomically Thin Carbon Films*, **306**, 666 (2016).

[48] Y. Huang, E. Sutter, N. N. Shi, J. Zheng, T. Yang, D. Englund, H. J. Gao, and P. Sutter, *Reliable Exfoliation of Large-Area High-Quality Flakes of Graphene and Other Two-Dimensional Materials*, ACS Nano **9**, 10612 (2015).

[49] J. W. Roh, J. S. Yang, S. H. Ok, D. H. Woo, Y. T. Byun, Y. M. Jhon, T. Mizumoto, W. Y. Lee, and S. Lee, *Wafer bonding between InP and Ce:YIG(CeY 2 Fe 5 O 12) using O 2 plasma surface activation for an integrated optical waveguide isolator*, in *Integrated Optics: Devices, Materials, and Technologies X*, volume 6123, page 612316, 2006.

[50] V. Masteika, J. Kowal, N. S. J. Braithwaite, and T. Rogers, *A Review of Hydrophilic Silicon Wafer Bonding*, ECS Journal of Solid State Science and Technology **3**, Q42 (2014).

[51] P. Amirfeiz, S. Bengtsson, M. Bergh, E. Zanghellini, and L. Börjesson, *Formation of Silicon Structures by Plasma-Activated Wafer Bonding*, Journal of The Electrochemical Society **147**, 2693 (2000).

[52] Y. Huang et al., *Universal mechanical exfoliation of large-area 2D crystals*, Nature Communications **11** (2020).

[53] M. Velický, G. E. Donnelly, W. R. Hendren, S. McFarland, D. Scullion, W. J. Debenedetti, G. C. Correa, Y. Han, A. J. Wain, M. A. Hines, D. A. Muller, K. S. Novoselov, H. D. Abruna, R. M. Bowman, E. J. Santos, and F. Huang, *Mechanism of Gold-Assisted Exfoliation of Centimeter-Sized Transition-Metal Dichalcogenide Monolayers*, ACS Nano (2018).

Appendix A

Quantitative Data Acquisition Using Image J

This appendix explains the extraction of quantitative data from microscope images. Namely, we obtain the cleaving yields as defined in eq. 5.1 (main text) and we try to find a correlation between flake thickness and optical contrast. We illustrate the process with a particular flake obtained using the optimized RIE parameters (table 5.1) to exfoliate a Bi-2212 parent flake onto a Si/SiO_2 substrate.

Figure A.1 shows the microscope images obtained during the exfoliation process. **a)-** A piece of tape containing the parent flake is stuck onto the cleaned Si/SiO_2 substrate. **b)-** After heating the substrate+tape system for 2 minutes at 100°C, the tape is removed leaving several flakes stuck to the substrate. **c)-** Finally, we stick the used tape into a new substrate to verify that the flakes in step b) were indeed cleaved and not transferred (see Fig. 5.3 in the main text).

The free software Image J (`https://imagej.net/Downloads`) can be used to analyze the three images in Fig. A.1. We briefly remind that an rgb image is simply a matrix of NxN pixels, where each pixel is associated with an array (r,g,b) that denotes the intensity of red, blue, and green colors of the pixel. The intensity of a particular pixel can be defined as:

$$I = (r + g + b)/3 \tag{A.1}$$

ranging from 0 to 255. A homogeneous flake has a constant value of intensity that will correlate with its thickness and differ from the intensity of the substrate.

In order to remove the effect of inhomogeneous illumination and to

compare flake intensities from different images, we define the contrast difference:

$$C = \frac{I_{flake} - I_{substrate}}{I_{flake} + I_{substrate}}. \tag{A.2}$$

The contrast difference allows us to set a threshold value C_{th} in order to automatically identify the different flakes. This threshold is used to create a mask by setting all the pixels with $|C| > C_{th}$ to 1 and all the remaining to 0. The contour of such masks is shown in Fig. A.2.

Once the mask is created, it can be used to calculate the contrast and area(# of pixels) of each flake. The area of the parent flake, together with the area of the cleaved flakes can be used to calculate the cleaving yield :

$$Yield = \frac{\text{Area of the parent flake}}{\sum_i \text{Area of cleaved flake}_i}. \tag{A.3}$$

The flakes in steps **a)** and **b)** of Fig. A.1 are frequently too thick leading to saturated values of the contrast that prevent us to obtain further information. However, the cleaved flakes in step **c** have different contrasts depending on their thickness.

Some layered materials like graphite display linear correlations between the optical contrast and the thickness of the few-layer flakes. However, in general, the correlation between optical contrast and thickness is not trivial. Figure A.3 shows an experimental curve relating the optical contrast of 20 different flakes to their thickness as measured using a profilometer. The relation between these two magnitudes is not single-valued and therefore does not allow for thickness identification from the optical contrast. Similar curves for the red, blue, and green channels might reveal an easier function relating thickness and contrast that could allow for unambiguous identification.

Version of March 24, 2021– Created March 24, 2021 - 12:07

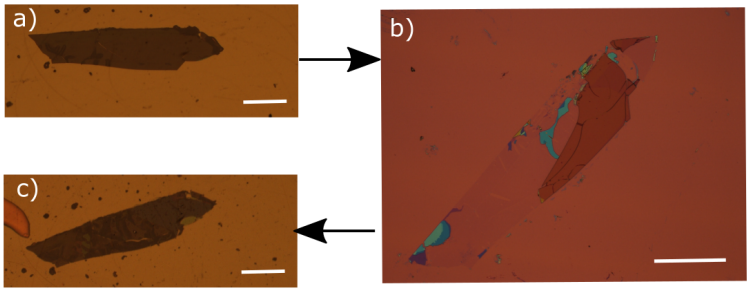

Figure A.1: *Original microscope images obtained* ***a)-*** *right after stamping the parent flake,* ***b)-*** *after removing the tape and* ***c)-*** *after sticking the tape into a new substrate. The white bar corresponds to* $200\mu m$

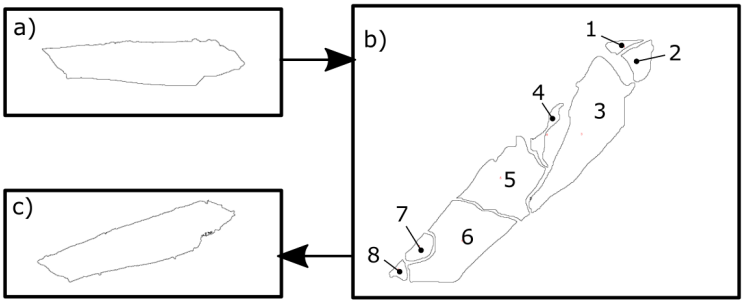

Figure A.2: *Masks obtained using the "Huang" auto-threshold algorithm in Image J for the images in Fig. A.1. The algorithm is able to select all the relevant cleaved flakes.*

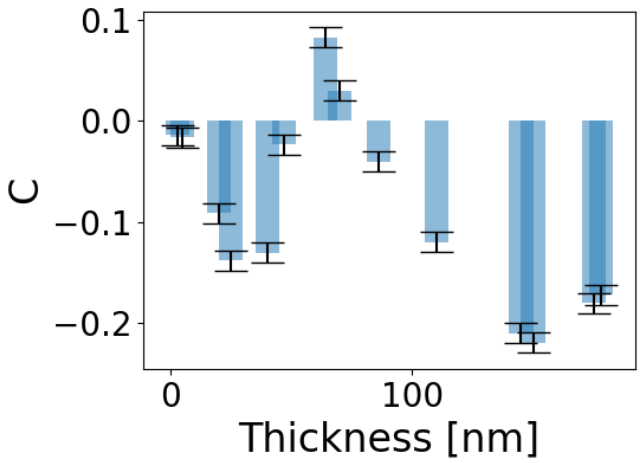

Figure A.3: *Correlation between optical contrast as defined in eq. A.2 and flake thickness as measured with the profilometer for 15 different flakes. The error of the profilometer was around 2nm and the error in the contrast was calculated from the standard deviation of the contrast of all the pixels within a flake.*